# The Physical Structure and Behavior of the California Current System

Lionel Renault*[1], James C. McWilliams*, Alexandre Jousse*, Curtis Deutsch†, Hartmut Frenzel†, Faycal Kessouri*#, and Ru Chen*

* Department of Atmospheric and Oceanic Sciences, University of California, Los Angeles, CA 90095-1565

† University of Washington, School of Oceanography, Box 357940, Seattle, WA 98195-7940

# Southern California Coastal Water Research Project, 3535 Harbor Blvd, Suite 110, Costa Mesa, CA 92626

February 6, 2020

**Abstract**

This paper is the first of two that present a 16-year reanalysis solution from a coupled physical and biogeochemical model of the California Current System (CCS) along the U. S. West Coast and validate the solution with respect to mean and seasonal fields and, to a lesser degree, eddy variability. Its companion paper is Deutsch et al. (2019a). The intent is to construct and demonstrate a modeling tool that will be used for mechanistic explanations, attributive causal assessments, and forecasts of future evolution for circulation and biogeochemistry, with particular attention to the increasing oceanic stratification, deoxygenation, and acidification. A well-resolved mesoscale ($dx = 4$ km) simulation of the CCS circulation is made with the Regional Oceanic Modeling System over a reanalysis period of 16 years from 1995 to 2010. The oceanic solution is forced by a high-resolution ($dx = 6$ km) regional configuration of the Weather and Research Forecast (WRF) atmospheric model. Both of these high-resolution regional oceanic and atmospheric simulations are forced by lateral open boundary conditions taken from larger-domain, coarser-resolution parent simulations that themselves have boundary conditions from the Mercator and Climate Forecast System reanalyses, respectively. We first show good agreement between the simulated atmospheric forcing of the ocean and satellite observations for the spatial patterns and seasonal variability of the cloud cover and for the surface fluxes of momentum, heat, and freshwater. The simulated oceanic physical fields are then evaluated with satellite and *in situ* observations. The simulation reproduces the main structure of the climatological upwelling front and cross-shore isopycnal slopes, the mean current patterns (including the California Undercurrent), and the seasonal and interannual variability. It also shows agreement between the mesoscale eddy activity and the wind-work energy exchange between the ocean and atmosphere modulated by influences of surface current on surface stress. Finally, the impact of using a high frequency wind forcing is assessed for the importance of synoptic wind variability to realistically represent oceanic mesoscale activity and ageostrophic inertial currents.

[1]Corresponding author: lrenault@atmos.ucla.edu

# 1 Introduction

Subtropical eastern boundary upwelling systems like the California Current System (CCS) are among the biologically most productive coastal environments (Carr and Kearns, 2003), supporting some of the world's major fisheries (FAO, 2009). Seasonal upwelling (mainly during spring and summer) of deep nutrient-rich water maintains high rates of productivity over broad scales (*e.g.,* Chavez and Messie (2009)). Additionally, coastal currents and oceanic mesoscale variability contribute to cross-shore exchange of heat, salt, and biogeochemical materials between the open and coastal oceans as well as the surface layer and interior (Hickey, 1998; Capet et al., 2008a; Gruber et al., 2011; Renault et al., 2012, 2016a).

The seasonal upwelling introduces water with low dissolved oxygen and low pH (*i.e.,* a below-critical carbonate saturation state) into the surface waters (Chan et al., 2008; Feely et al., 2008; Gruber et al., 2012), making this region more prone to hypoxia and acidification (Feely et al., 2018; Gruber et al., 2012). Shoaling of deep, low-oxygen and low-pH waters is particularly pertinent in the CCS because the eastern Pacific Ocean contains the worlds largest mid-depth Oxygen Minimum Zone (OMZ). This OMZ has been expanding (*e.g.,* Stramma et al. (2010)), which makes the coast more susceptible to hypoxic intrusions onto its narrow continental shelf (*e.g.,* Pennington et al. (2006)). The entire CCS is subject to large-scale climate changes (*e.g.,* Stramma et al. (2012); Bopp et al. (2015); Garcia-Reyes et al. (2105)) that include deoxygenation caused in part by increased density stratification through anomalous greenhouse heating and the acidification due to anthropogenic $CO_2$ invasion. These global influences may be exacerbated in coastal regions by pollutants deposited from the atmosphere (*e.g.,* nitric and sulfuric acid), from urban wastewater effluents, and from riverine eutrophication and other contaminants. Multi-decadal declines in oxygen leading to hypoxia have also been observed in the coastal water off southern California and Oregon and have altered the proportions of biologically important nutrients. Dramatic responses to these perturbations have already been observed in species that form critical links in the food web (*e.g.,* pteropods for ocean acidification (Bednarsek and Ohman, 2015; Bednarsek et al., 2017) and benthic species for hypoxia (Grantham et al., 2004; Feely et al., 2018)).

Regional upwelling patterns and eddies are important influences on the ecosystem. Mesoscale eddies, induced by baroclinic and barotropic instabilities of the wind-driven currents (*e.g.,* Marchesiello et al. (2003)), are present everywhere in the world ocean and play a key role in many oceanic processes. Many studies have shown their crucial role in the transport of heat and freshwater (*e.g.,* Wunsch (1999); Dong et al. (2014)) and biogeochemical materials (McGillicuddy, 2016). In the open ocean, mesoscale processes can enhance the biological production by increasing the surface concentration of limiting nutrients (McGillicuddy, 2016). In eastern boundary upwelling systems, eddies are a limiting factor that reduces the autotrophic primary production by fluxing unconsumed surface nutrients beneath the euphotic layer ("eddy quenching") (Gruber et al., 2011; Renault et al., 2016a). As shown by Renault et al. (2016b,a), a realistic representation of the slackening of the wind toward the coast (*i.e.,* wind drop-off) is influential for the mean and mesoscale currents, the primary production, and interior oxygen levels (Deutsch et al., 2019b).

While equilibrium regional oceanic circulation models have been successfully employed for more than a decade in the CCS (Marchesiello et al., 2003; Capet et al., 2008a; Veneziani et al., 2009), no previous simulation has been made over a long time period using high-resolution spatial and temporal atmospheric forcing that includes the effects of wind drop-off (*i.e.,* the cross-shore profile of decreasing wind speed toward the coast), current feedback on the surface stress (causing

a dampening of the mesoscale activity; Renault et al. (2016d)), and high-frequency wind fluctuations. In this paper and its biogeochemical companion (Deutsch et al., 2019a), the Regional Oceanic Modeling System (ROMS) is implemented over the CCS and is forced by the atmosphere with a regional configuration of the Weather Research Forecast (WRF) model for the period 1995-2010. The main objectives are to characterize and validate the mean seasonal behavior of the CCS circulation with good mesoscale resolution in both the ocean ($dx = 4$ km) and atmosphere ($dx = 6$ km). This also provides an assessment of the importance of synoptic wind forcing on the mean and mesoscale currents as well as on the inertial currents. Overall, it provides a more comprehensive validation assessment than is customary, both to establish the credentials of this particular model for its intended applications (mostly biogeochemical and ecological) and to provide an example of the state of the art for realistic regional simulations.

The datasets and the model components, set-up, and analyses methodology are described in Sec. 2. In Sec. 3 the atmospheric forcing is evaluated with respect to satellite observations of clouds, surface heat, freshwater, and momentum fluxes. In Sec. 4 the oceanic simulation is evaluated with respect to both satellite products and previous analyses, and the importance of the high frequency atmospheric forcing is assessed. For all these fields explanations of the resulting patterns are given based on our present understanding. The results are discussed and summarized in Sec. 5.

# 2 Model Configurations and Analysis Methods

The numerical models and configurations are similar to those in Renault et al. (2016d), where they are described more fully. Furthermore, the model code including its parameter settings are available through the GitHub repository (see the remark at the end of the paper).

## 2.1 The Regional Oceanic Modeling System (ROMS)

The oceanic simulations are made with ROMS (Shchepetkin and McWilliams, 2005; Shchepetkin, 2015). As in Renault et al. (2016d), the primary U. S. West Coast (USW4) simulation domain extends from 144.7°W to 112.5°W and from 22.7°N to 51.1°N. Its horizontal grid is 437 x 662 points with a resolution of $dx = 4$ km, and it has 60 terrain- and surface-following sigma levels in the vertical with stretching parameters $h_{cline} = 250$ m, and $\theta_b = 3.0$, and $\theta_s = 6$ (Shchepetkin and McWilliams, 2009).

Initial and horizontal boundary data for $T$, $S$, surface elevation, and horizontal velocity are taken from the quarter-degree, daily-averaged Mercator Glorys2V3 product (*http://www.myocean.eu*), and applied to the outer boundary of a $dx = 12$ km solution, which spans a larger domain and serves as a parent grid for the USW4 solution. To improve the water mass representation, in particular the density distribution, the Mercator data are corrected using the mean monthly climatology from the World Ocean Atlas (WOA) (Locarnini et al., 2013; Zweng et al., 2013) over the period 1995-2004. As we shall see in Sec. 4.2, the model does exhibit a mean bias in $S$ (*e.g.,* the geographical distribution on an interior density surface), and our understanding is that this mostly is inherited from WOA due to the sparsity of interior hydrographic observations used to determine an accurate mean state around the model boundaries.[2]

[2] In retrospect, a better result might have occurred had we done a density-space correction of the boundary mean

The surface turbulent evaporation, heat, and momentum fluxes are estimated using bulk formulae (Large, 2006), and the atmospheric surface fields are derived from an uncoupled WRF simulation (Sec. 2.2), along with the precipitation and downwelling radiation; for these surface fluxes the temporal sampling interval is one hour (1H; see Sec. 4.6 for the sensitivity to this interval). As in Lemarié et al. (2012), the river-runoff forcing dataset we use is a monthly climatology from Dai et al. (2009). River runoff is included off-line as surface precipitation and is spread using a Gaussian distribution over the grid cells that fall within the range from the coast to 150 km offshore; this excludes a detailed representation of river plumes.

When forced with bulk formulae, uncoupled oceanic simulations often estimate the surface stress using the wind vector $\boldsymbol{U_a}$ (*e.g.,* at 10 m height). As shown by *e.g.,* Dewar and Flierl (1987); Duhaut and Straub (2006); Eden and Dietze (2009); Renault et al. (2016c), such simulations overestimate the mesoscale activity because of their lack of a current feedback. At the mesoscale the current feedback to the atmosphere induces a sink of energy from the currents to the atmosphere, which causes a large dampening of the mesoscale activity (by $\approx 40\%$ for the U.S. West coast; Seo et al. (2015); Renault et al. (2016d)). Alternatively, if the relative velocity difference between the surface wind and current $\boldsymbol{U_r}$ is used in the bulk formula, $\boldsymbol{\tau} = \rho_a C_d \left|\boldsymbol{U_r}\right| \boldsymbol{U_r}$ (with $\rho_a$ the surface air density and $C_d$ the drag coefficient), an opposite bias arises in an uncoupled ocean model: the mesoscale activity is underestimated because the wind response to the weakened currents through this stress feedback should partially re-energize the atmosphere, hence also the mesoscale currents. Renault et al. (2016d) suggest using a simple parameterization based on the current-wind coupling coefficient $s_w$, estimated from a coupled simulation as the slope between the mesoscale current vorticity and the mesoscale surface stress curl. The atmospheric re-energization is then expressed as

$$\boldsymbol{U'_a} = s_w \boldsymbol{U_o}\,, \tag{1}$$

where $\boldsymbol{U_o}$ is the surface current, $\boldsymbol{U'_a}$ is the wind response to $\boldsymbol{U_o}$, and $s_w$ is a statistical regression coefficient. The surface stress, therefore, is computed using a bulk drag formula,

$$\tau = \rho_a C_D \left|\boldsymbol{U_r}\right| \boldsymbol{U_r}\,, \tag{2}$$

with a parameterized relative velocity, $\boldsymbol{U_r}$:

$$\boldsymbol{U_r} \;=\; \boldsymbol{U_a} + \boldsymbol{U'_a} - \boldsymbol{U_o} \;=\; \boldsymbol{U_a} - \,(1 - \,s_w)\boldsymbol{U_o}\,, \tag{3}$$

where $\boldsymbol{U_a}$ is the surface wind from an uncoupled atmospheric product. For the CCS region, $s_w = 0.23 \pm 0.1$ (Renault et al., 2016d). This simple parameterization roughly mimics the wind response to the current feedback. Although such a parameterization presents some limitations (*i.e.,* in this study $s_w$ is constant, so does not take into account the seasonal cycle, the atmospheric boundary layer dependency, nor the global-scale geographic variation of $s_w$), but it does lead to approximately the expected damping and re-energization of the mesoscale currents. The alternative to such a parameterization is full ocean-atmosphere coupling, which is much more computationally expensive.

The statistically equilibrated solution USW4 is integrated over the period 1995-2010 after a spin up of 1 year starting from a larger-domain ROMS parent solution with $dx = 12$ km.

$T - S$ values, as is done for the biogeochemical properties (Deutsch et al., 2019a), but this is unlikely to overcome sampling error from data sparseness. A more elaborate procedure would be to adjust the boundary data to reduce interior bias, but this would be a form of data assimilation, which we otherwise have avoided.

## 2.2 The Weather Research and Forecast Model (WRF)

WRF (version 3.6.1; Skamarock et al. (2008)) is implemented in a configuration with two grids, similar to Renault et al. (2016b). The WRF domains are slightly larger than the ROMS domains to avoid the effect of the WRF boundary sponge (4 grid points wide). It has horizontal resolutions of 18 km and 6 km, respectively, using only the latter over the USW4 domain. The model is initialized with the Climate Forecast System Reanalysis (CFSR with $\approx 40$ km horizontal resolution; Saha et al. (2010)) from 1 January 1994 and integrated for 17 years with time-dependent boundary conditions interpolated from the same six-hourly reanalysis. Forty vertical levels are used, with half of them in the lowest $1.5$ km, as in Renault et al. (2016b). The model configuration is set-up with the same parameterizations as in Renault et al. (2016b) except that the WRF Single-Moment, 6-class microphysics scheme (Hong and Lim, 2006) is modified to take into account the spatial and seasonal variations of the droplet concentration (Jousse et al., 2016). Its Sea Surface Temperature (SST) forcing is derived from the Ostia one-day product (Stark et al., 2007) that has a spatial resolution of 5 km. The inner-nested domain (WRF6) is initialized from the outer solution (WRF18) on 1 April 1994 and integrated for 17 years. Only the period 1995-2010 is used in the model evaluations.

## 2.3 Analysis Methods

The numerical outputs for the solutions are daily averages, except when assessing the high frequency forcing importance where hourly averages outputs are saved. The winter, spring, summer, and fall seasons correspond to the months January-March, April-June, July-September, and October-December, respectively. To assess the realism of the oceanic and atmospheric solutions, several sub-regions are considered (Fig. 1): see the separate boxes for southern California (South), central California (Central), and northern California plus Oregon and Washington (North). Additionally, when the the data have a spatial resolution that is high enough to consider a coastal region (*i.e.,* $dx < 1°$) and do not have too large a nearshore bias zone (*e.g.,* QuikSCAT products usually have a coastal blind zone about 30-50 km wide), both Nearshore and Offshore sub-boxes are also considered. The mean $\overline{(\cdot)}$ is defined with respect to the full time average (1995-2010) and is done separately for each season; the prime $(\cdot)'$ denotes a deviation from the mean.

The oceanic geostrophic surface currents are estimated using daily-averaged sea surface height:

$$u_{og} = -\frac{g}{f}\frac{\partial h}{\partial y}\,, \tag{4}$$

and

$$v_{og} = \frac{g}{f}\frac{\partial h}{\partial x}\,, \tag{5}$$

where $u_{og}$ and $v_{og}$ are zonal and meridional geostrophic currents, $g$ is gravitational acceleration, $f$ is Coriolis frequency, and $h$ is sea-surface height.

Following the method described in Renault et al. (2016c), the total wind-work is defined as

$$FK = \frac{1}{\rho_0}\left(\overline{\tau_x\, u_o} + \overline{\tau_y\, v_o}\right), \tag{6}$$

where $u_o$ and $v_o$ are the zonal and meridional surface currents, $\tau_x$ and $\tau_y$ are the zonal and meridional surface stresses, and $\rho_0$ is the mean seawater density. Substituting the decomposition of (4)

and (5) into (6), the total wind-works on the geostrophic and ageostrophic flow are

$$FK_g = \frac{1}{\rho_0}\left(\overline{\tau_x\, u_{og}} + \overline{\tau_y\, v_{og}}\right), \tag{7}$$

and

$$FK_a = \frac{1}{\rho_0}\left(\overline{\tau_x\, u_{oa}} + \overline{\tau_y\, v_{oa}}\right), \tag{8}$$

where $u_{oa}$ and $v_{oa}$ are the zonal and meridional components of ageostrophic velocities, respectively. The wind -works $FK_g$ and $FK_a$ can be split into their mean ($F_mK_{mg}$ and $F_mK_{ma}$) and eddy parts ($F_eK_{eg}$ and $F_eK_{ea}$):

- mean geostrophic wind-work,

$$F_mK_{mg} = \frac{1}{\rho_0}\left(\overline{\tau_x}\,\overline{u_{og}} + \overline{\tau_y}\,\overline{v_{og}}\right); \tag{9}$$

- mean ageostrophic wind-work,

$$F_mK_{ma} = \frac{1}{\rho_0}\left(\overline{\tau_x}\,\overline{u_{oa}} + \overline{\tau_y}\,\overline{v_{oa}}\right); \tag{10}$$

- geostrophic eddy wind-work,

$$F_eK_{eg} = \frac{1}{\rho_0}\left(\overline{\tau'_x\, u'_{og}} + \overline{\tau'_y\, v'_{og}}\right); \tag{11}$$

- ageostrophic eddy wind-work,

$$F_eK_{ea} = \frac{1}{\rho_0}\left(\overline{\tau'_x\, u'_{oa}} + \overline{\tau'_y\, v'_{oa}}\right). \tag{12}$$

As in Stern (1975), Marchesiello et al. (2003), and Renault et al. (2016d), we evaluate the following relevant eddy-mean energy conversion terms:

- barotropic (horizontal Reynolds stress) kinetic energy conversion $K_mK_e$,

$$K_mK_e = -\int_z \left(\overline{u'_o\, u'_o}\frac{\partial \overline{u_o}}{\partial x} + \overline{u'_o\, v'_o}\frac{\partial \overline{u_o}}{\partial y} + \overline{u'_o\, w'}\frac{\partial \overline{u_o}}{\partial z} + \overline{v'_o\, u'_o}\frac{\partial \overline{v_o}}{\partial x} + \overline{v'_o\, v'_o}\frac{\partial \overline{v_o}}{\partial y} + \overline{v'_o\, w'}\frac{\partial \overline{v_o}}{\partial z}\right) dz \tag{13}$$

  (where $w$ is the vertical velocity and $x$, $y$, and $z$ are the zonal, meridional, and vertical coordinates, respectively) and

- eddy baroclinic potential-to-kinetic conversion $P_eK_e$,

$$P_eK_e = -\int_z \frac{g}{\rho_0}\,\overline{\rho'\, w'}\, dz\,. \tag{14}$$

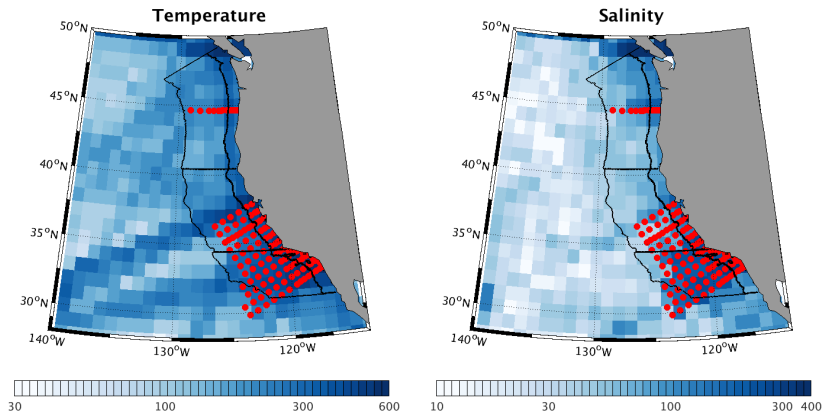


Figure 1: Data density of temperature and salinity measurements in World Ocean Database. The black lines indicate the box areas used to evaluate the simulations with respect to the observations. Three alongshore domains are assessed: South, Central, and North. When the data have a high-enough spatial resolution to assess a coastal region (*i.e.,* more than two cross-shore valid data), Nearshore and Offshore boxes are also considered with the meridional boundary line, also in black. The red lines indicate the CalCOFI data and the Newport hydrographic line.

$F_m K_{mg}$ represents the transfer of energy from mean surface wind-forcing to mean geostrophic kinetic energy; $F_m K_{ma}$ represents the transfer of energy from mean surface wind-forcing to mean ageostrophic kinetic energy; $F_e K_{eg}$ represents the transfer of energy from surface wind-forcing anomalies to geostrophic EKE; $F_e K_{ea}$ represents the transfer of energy from surface wind-forcing anomalies to ageostrophic EKE; $K_m K_e$ represents the barotropic conversion from mean kinetic energy to EKE; and $P_e K_e$ represents the baroclinic conversion from eddy available potential energy to EKE. We compute those conversion terms at each model grid point. The wind-work is estimated at the free surface, while the barotropic and baroclinic conversion terms are integrated over the whole water column.

## 2.4 Observational Datasets

Satellite and *in situ* observations are used to evaluate the realism of both the atmospheric and oceanic simulations. Because of intermittent sampling with different instruments, we do not insist on exact time correspondences in computing climiatological averages. To evaluate the performance of the atmospheric simulation in terms of cloud cover, we use remote sensing data retrieved from the Moderate-resolution Imaging Spectrometer level 2 data (MODIS; Platnick et al. (2003)). We use data from the Terra satellite, which is available twice daily around 10:30 am/pm local time, beginning in the year 2000. The Forcing for Coordinated Ocean-ice Reference Experiments 2 (CORE; Large and Yeager (2009)) dataset is used to evaluate the surface heat and freshwater fluxes. It provides monthly surface fluxes at a spatial resolution of 1°. The monthly Global Precipitation Climatology Project (GPCP; Adler et al. (2003)) is also used to evaluate precipitation. It has a spatial resolution of 1°. The surface stress data is from the Scatterometer Climatology of Ocean

Winds (SCOW; Risien and Chelton (2008)) product based on the QuikSCAT satellite scatterometer. It provides monthly data at a 0.25°resolution. To compute the wind-work, the surface stress daily product processed by the Centre ERS dArchivage et de Traitement (CERSAT; Bentamy and Fillon (2012)) is used. It provides daily surface stress at a spatial resolution of 25 km. SST forcing is derived from the Ostia daily product (Stark et al., 2007) that has a spatial resolution of 5 km. We use data from the California Cooperative Oceanic Fisheries Investigations (CalCOFI) (*e.g.,* Bograd et al. (2003)). Since 1950 hydrographic stations have been repeatedly but irregularly sampled on a geographically fixed grid. In this study line 80 (off Pt. Conception; 34°N) is used to estimate a seasonal climatology of temperature, salinity, and density, respectively, to validate the simulation from 1995 to 2010. The temperature, salinity, and density are further evaluated using the World Ocean Database 2013 (WOD13, Locarnini et al. (2013); Zweng et al. (2013)). Its fields have a resolution of 25 km and extend from the surface to the bottom of the ocean. The WOD13 dataset for that period includes the CalCOFI data and the Newport hydrographic line. The CSIRO (Commonwealth Scientific and Industrial Research Organization) Atlas of Regional Seas (CARS) climatology (Ridgway et al., 2002) provides an estimate of the monthly climatology of the Mixed Layer Depth (MLD) using a temperature threshold of $\Delta\Theta = 0.2$ °and $\Delta\sigma_\theta = 0.03$ kg m$^{-3}$. Finally, the CNES-CLS13 dataset (Rio et al., 2014) is used to evaluate the simulated mean sea surface height and to estimate the geostrophic wind-work. It is a combination of GRACE satellite data, altimetry, and *in situ* measurements with a spatial resolution of 25 km in the analysis product. The Archiving, Validation, and Interpretation of Satellite Oceanographic Data (AVISO) dataset (Ducet et al., 2000) is used to evaluate the mesoscale activity simulated by USW4 and to estimate geostrophic wind-work. It provides the daily sea level anomaly at a resolution of 25 km.

# 3 Atmospheric Fields

## 3.1 Cloud Cover and Shortwave Radiation

The representation of clouds and their radiative properties is a common difficulty for both global and regional climate models in eastern boundary upwelling regions (Nam et al., 2012; Wyant et al., 2010; Zermeño-Díaz et al., 2015). The difficulty is at least partially attributable to approximate parameterizations of processes governing the stratocumulus that dominate these regions due to the combination of large-scale tropospheric downwelling, low humidity, and a cold oceanic SST adjacent to a generally warmer continent. WRF offers choices among various physical parameterizations; here we make our choice in accordance with previous work where an optimized combination of parameterizations was established in WRF for a stratocumulus region (Jousse et al., 2016). In particular, this combination (Sec. 2.2) minimize stratocumulus biases, and for the present WRF simulations similar sensitivity tests confirm the previous choices. We also perform sensitivity tests for the surface shortwave radiation scheme (not done in Jousse et al. (2016)). Our results show a better performance of the Goddard Shortwave scheme (Chou and Suarez, 1994) in comparison to the Dudhia scheme (Dudhia, 1989). We prescribe the observed spatial variability and seasonality for the cloud droplet concentration number in the microphysics parameterization scheme WSM6. This modeling strategy minimizes biases in the liquid water path over the northeast Pacific.

To diagnose the cloud cover in our simulations, we use a Total Water Path (TWP, *i.e.,* the sum of the ice and liquid water paths) with a threshold value of 5 g m$^{-2}$ (*i.e.,* cloud cover is 100% if

$TWP > 5$ g m$^{-2}$, else it is set to zero). This definition attempts to mimic the fractional cloudiness retrieved from a satellite sensor; see Jousse et al. (2016) for further details. The results of the comparison between MODIS and WRF cloud cover are in Fig. 2. Overall there is good agreement between them in terms of spatial variability and the seasonal cycle for the different domains of interests, in both the Nearshore and Offshore boxes (Fig. 1), but there is a slight overestimation of cloud cover by WRF in comparison to MODIS. This overestimation may be at least partially attributable to the resolution mismatch between the MODIS cloud mask (1-5 km) and the WRF resolution (*i.e.,* a grid size of 6 km and an effective resolution of $\approx$ 30 km; Skamarock et al. (2008)). There is also a slight underestimation of the cloud cover by WRF in both the Central and South Nearshore boxes during the summer season (by about 10%; Fig. 3). One likely contributor to this bias is the horizontal diffusion scheme used in WRF version 3.6. This scheme is computed on terrain-influenced model surfaces (*i.e.,* eta levels). Similar to what has been recently shown for a stable cold pool (Wilson and Fovell, 2016), such a treatment tends to mix air up and down the coastal mountain slopes in the Nearshore region. Thus, during the summer months, when the planetary boundary layer is generally lower than the coastal orographic elevation (*i.e.,* about 500 m), this type of diffusion scheme produces a spurious mixing between the marine layer and the inversion layer above. This tends to dry and warm the marine boundary layer, which lowers the boundary relative humidity and thus results in a reduction of the cloud cover. Using a more recent version of WRF (version 3.7) that computes horizontal diffusion on geopotential levels, the cloud cover underestimations are reduced in the coastal regions (not shown). Unfortunately, this version of WRF was not available at the time we generated our simulations; nevertheless, we consider these errors acceptable because they are only significant for the first one or two nearshore grid points. To sum up, WRF cloud cover estimates are approximately validated within the uncertainties of the remote sensor retrievals and the limitations of the method used to estimate the cloud cover in the model.

Surface net shortwave flux is a key component of the surface energy budget in the CCS. Figure 4 demonstrates the plausible WRF results for both spatial variability and seasonal cycle in all the regions of interests. There is a general increase in incident flux moving equatorward and, in the south, shoreward, modulated by the cloud cover. These results reflect the realism of the cloud macro-physical structure (*i.e.,* TWP) in the simulation (Jousse et al., 2016). Along the central California coast the underestimation of the cloud cover during summer (Fig. 3) leads to an overestimation of the mean shortwave flux, whereas there is an underestimation of the shortwave flux over the Southern California Bight caused by the overestimation of the cloud cover by 5-10 %. These biases are relatively small compared to global climate models (Richter, 2015).

## 3.2 Surface Heat Flux

The net surface heat flux is calculated in USW4 using the WRF solar radiation; 10 m wind; 2 m temperature and humidity fields; and SST. The resulting flux is evaluated with respect to the CORE dataset. Due to the upwelling and the cold coastal SST in the CCS, there is generally strong net heating of the ocean near the coast. Figure 5 shows the mean net surface heat flux and its seasonal variability in the different regions (*i.e.,* the alongshore boxes in Fig. 1). Here, we do not consider Offshore and Nearshore boxes because of the coarse spatial resolution of CORE (1°). Despite some bias compensations, there is an overall good agreement between the observations and the simulations both in term of spatial variability and seasonal cycle. In particular, the maximum of net

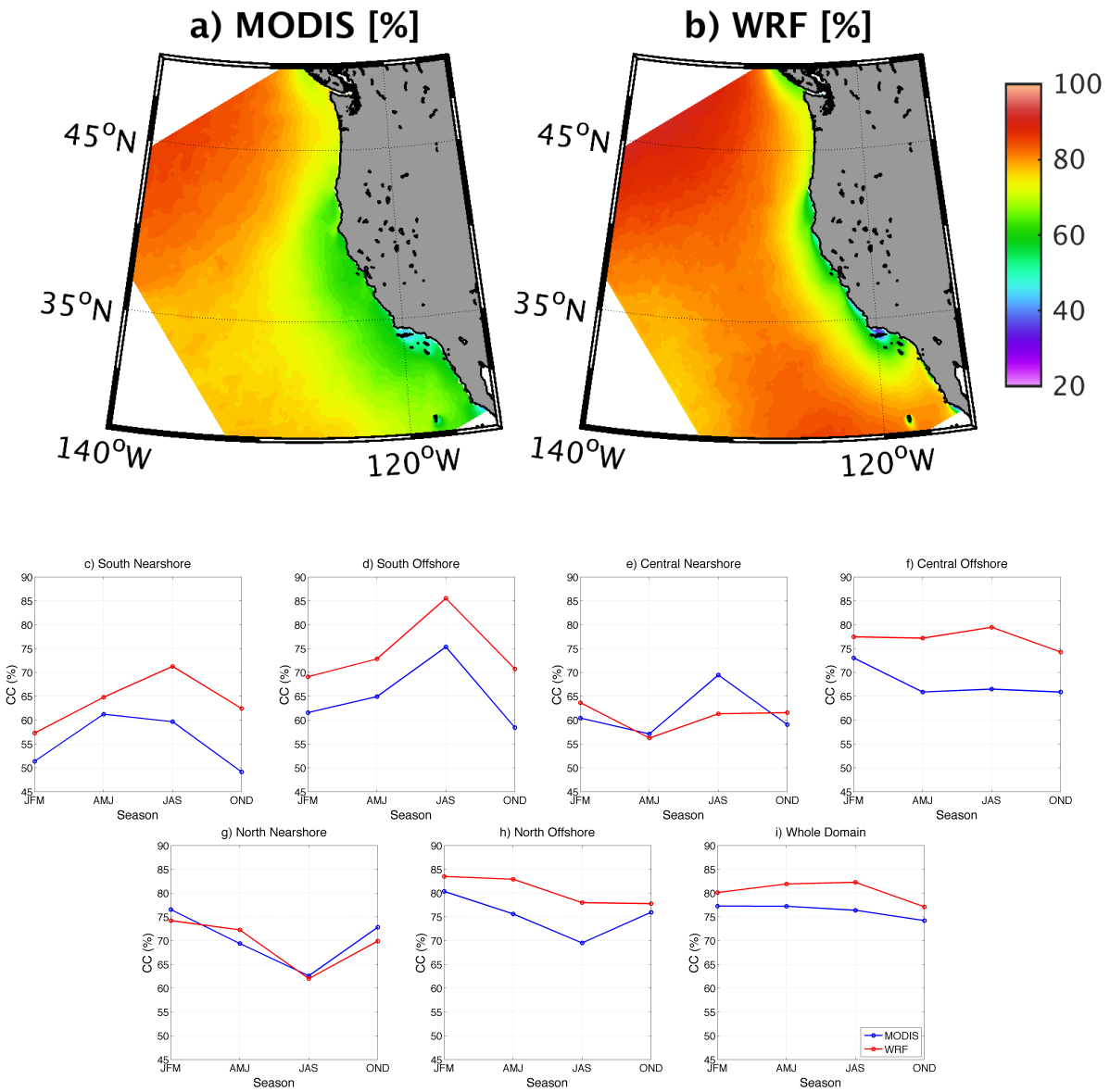


Figure 2: Mean Cloud Cover percentage estimated for the period 2000-2010 from (a) MODIS and (b) WRF. Panels (c), (d), (e), (f), (g), (h), and (i) represent the seasonal cloud cover variation over the same period from MODIS (blue) and USW4 (red) averaged over the boxes indicated in Fig. 1 or over the whole domain. WRF has a general good agreement with the observations and reproduces realistically the seasonal cycle of the cloud cover.

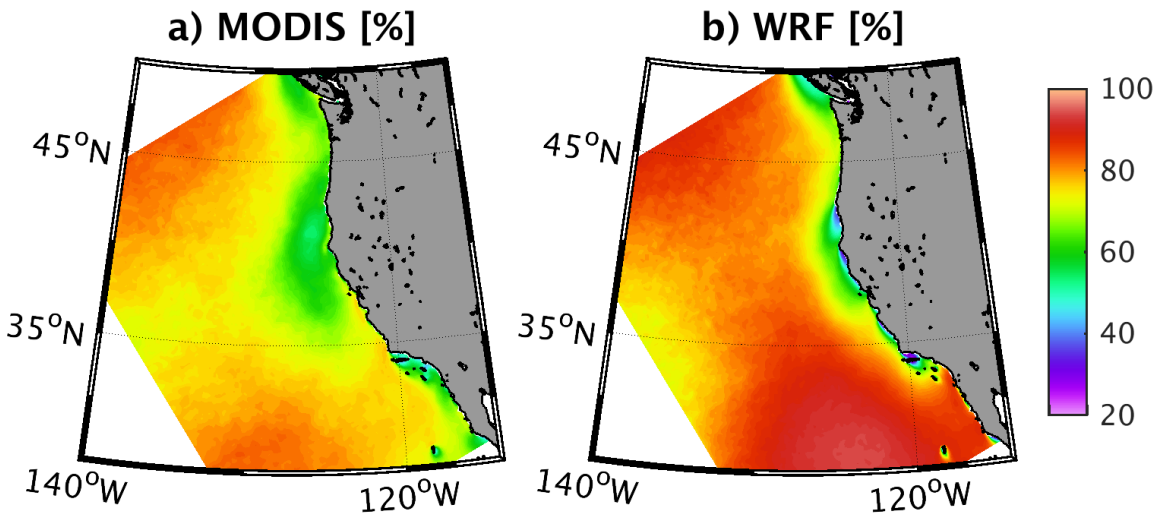


Figure 3: Mean cloud cover percentage estimated for the period 2000-2010 for the summer season with (a) MODIS, and (b) USW4. During summer the planetary boundary layer height is lower than the coastal orography (*i.e.,* $< 500$ m). The diffusion scheme in WRF produces a spurious mixing between the marine layer and the inversion layer located above, which dries and warms the marine boundary layer, hence reduces the cloud cover.

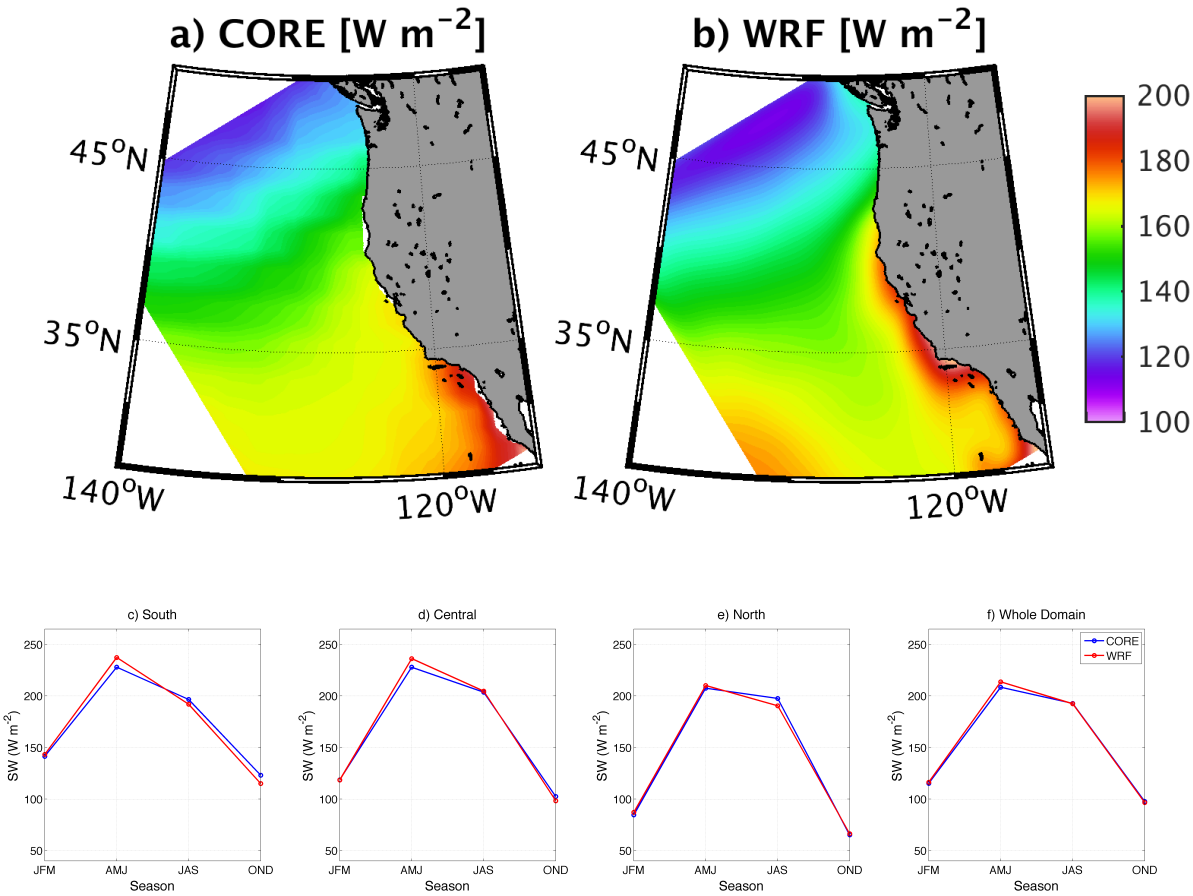


Figure 4: Mean shortwave radiation [W m$^{-2}$] estimated for the period 1995-2006 from (a) CORE and (b) USW4. Panels (c), (d), (e), and (f) represent the seasonal shortwave radiation variation estimated over the same period from CORE (blue) and WRF (red), averaged over the boxes indicated on Fig. 1 or over the whole domain. The realistic representation of the cloud cover and of the liquid water path in the model allows a good representation of the shortwave radiation.

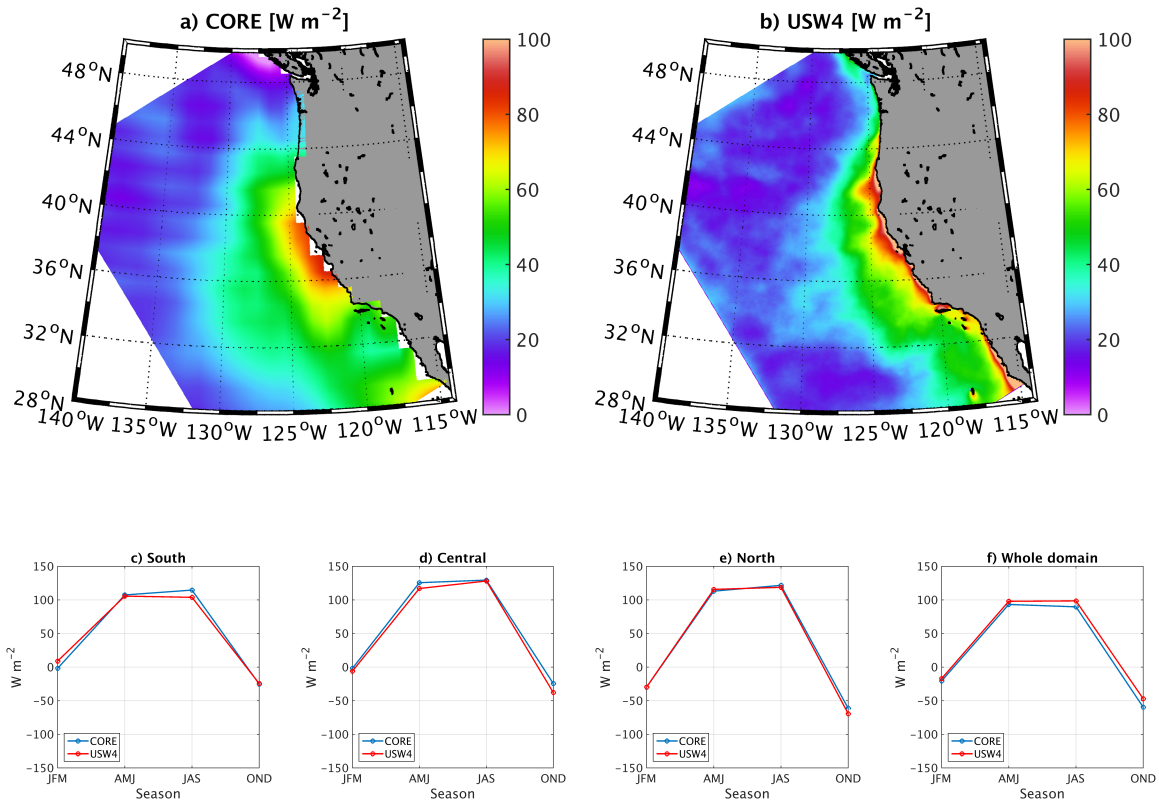


Figure 5: Mean net heat fluxes [W m$^{-2}$] from (a) CORE and (b) USW4 over the period 1995-2006. Panels (c), (d), (e), and (f) represent the seasonal evolution of the net heat fluxes over the same period from CORE (blue) and USW4 (red), averaged over the boxes indicated in Fig. 1 or over the whole domain.

heat flux in the Central box coast is well reproduced by USW4. Consistent with the overestimation of the cloud cover and the underestimation of the shortwave radiation, during the upwelling seasons (spring and summer), the largest bias is again located in the Southern California Bight, where the net surface heat flux is underestimated by 10 W m$^{-2}$. Along the central California coast, the cloud cover bias induces a positive bias in shortwave radiation that is mostly compensated for by a negative bias in longwave radiation (not shown). The turbulent (latent and sensible) heat fluxes exhibit less than a 7% error (*i.e.,* too large a latent heat flux), which is within the error range for the observations (Large and Yeager, 2009). Finally, near the coast in a band $\approx$ 30 km wide, the net heat flux is higher than in the observations, which probably reflects the coarser spatial resolution of CORE. The realistic representation of the net heat flux leads to a reasonably good estimate of the spatial and the seasonal variation of the SST (Sec. 4.1); however, as shown in Deutsch et al. (2019a), the shortwave flux bias along the California coast can induce a positive bias in chlorophyll through photosynthesis.

## 3.3 Surface Freshwater Flux

WRF and GPCP are in fairly good agreement for both the mean spatial pattern and seasonal cycle over our three alongshore regions (Fig. 6). Evaporation dominates toward the south over the warmer subtropical gyre, and precipitation dominates to the north, especially close to the coast; *i.e.,* there is more precipitation in the north during the winter months due to the storm tracks. WRF generally overestimates GPCP by about 0.5 to 1 mm day$^{-1}$. These differences are certainly not negligible values for the water budget. Nevertheless, they remain within the observational uncertainty range provided by the GPCP data. Moreover, due to their lack of sensitivity to drizzle, remote sensors are known to generally underestimate the precipitation produced by low clouds (Rapp et al., 2013). Because the CCS is substantially covered with low clouds, this may explain some of the discrepancies between WRF and GPCP (*n.b.,* similar results are found using CORE). The net freshwater flux (evaporation minus precipitation) is computed by USW4 by combining the precipitation from WRF and the evaporation estimated by bulk formulae from WRF's surface fields (Large, 2006). The overestimation of the precipitation is compensated for by an slight excess of evaporation (consistent with the latent heat flux bias), which leads to a realistic agreement of the net freshwater flux between USW4 and CORE (Fig. 7).

## 3.4 Surface Stress

Over the CCS the wind stress is mostly equatorward due to the offshore position of the atmospheric subtropical high, and this is the primary cause of offshore Ekman transport and coastal upwelling. This pattern is persistent in the South and Central boxes, with peak stresses near the coast in spring and summer. In the north the alongshore wind stress direction reverses seasonally.

The surface stress is calculated in USW4 with the Large (2006) bulk formulae as described in Sec. 2.1; the 10 m wind; and the 2 m temperature and humidity. Renault et al. (2016b) show a good agreement between the 10 m wind and the observations with a similar model configuration. Here, we evaluate the simulated surface stress with respect to SCOW. It compares well both in amplitude and direction, both the seasonality and the main gradients of the surface stress over the different regions of interest (Fig. 8). We do not consider separate Nearshore and Offshore boxes because, as noted by *e.g.,* Renault et al. (2009, 2016b), QuikSCAT data do not measure the stress within the first 50 km from the coast due to land contamination in the backscatter measurements (Chelton et al., 2004). The upwelling season in spring and summer is marked by a distinctive alongshore surface stress (up to 0.09 N m$^{-2}$), and the numerous capes and mountain ranges induce so-called expansion fans (Winant et al., 1988). The main discrepancies between SCOW and WRF occur close to the coast. In the simulation there is a coastal band where the surface stress is reduced compared to its offshore value (*i.e.,* the wind drop-off). Such a slackening of the wind is mainly caused by the presence of coastal orography, coastline shape, the difference between marine and terrestrial drag coefficients, and SST; this drop-off pattern is not well captured in QuikSCAT. An indirect validation of the wind drop-off is given by the oceanic response. A too-wide drop-off causes a poor representation of mean oceanic current structure and mesoscale activity (Renault et al., 2016b). Finally, the stress magnitude is slightly underestimated by USW4: the mean biases over the whole domain are 0.006 N m$^{-2}$ and 0.003 N m$^{-2}$ for the meridional and the zonal surface stress, respectively, *i.e.,* the same order of magnitude as the QuikSCAT surface stress error (Risien and Chelton, 2008). The least skillfully simulated region is again the Southern California Bight,

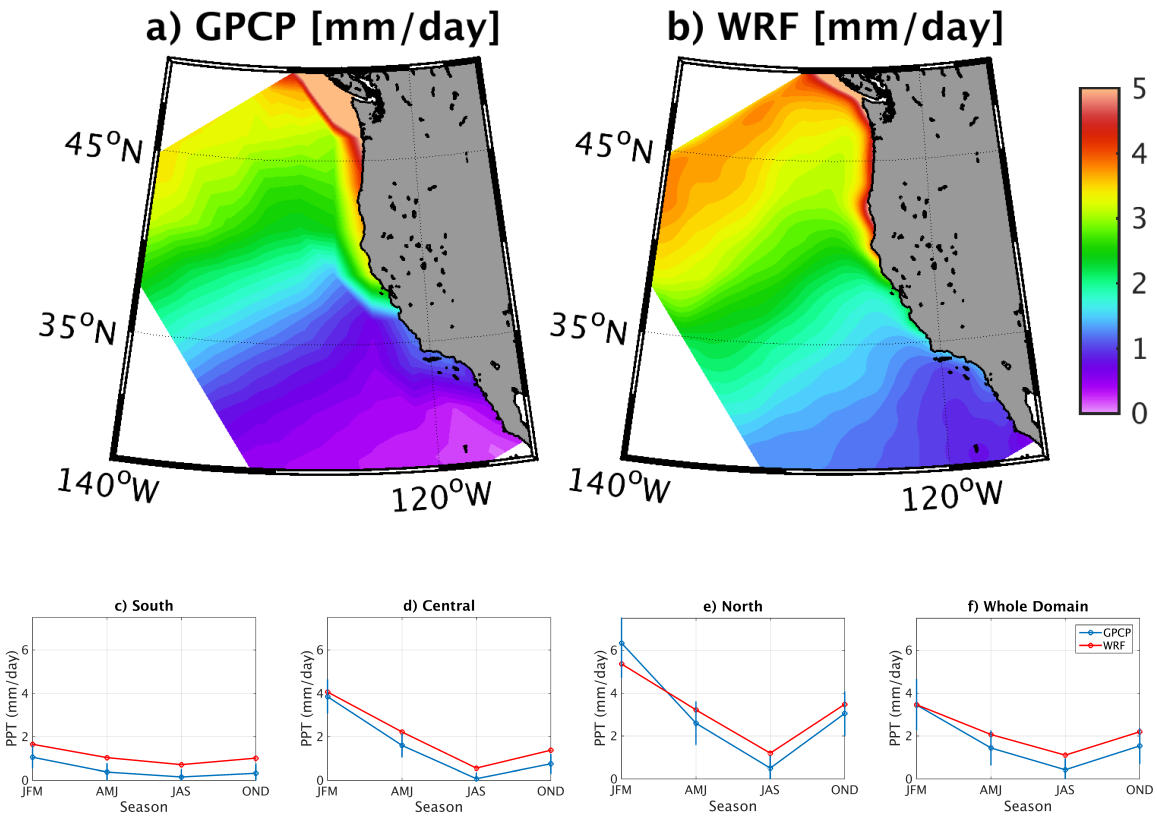


Figure 6: Mean precipitation [mm day$^{-1}$] from (a) GPCP and (b) WRF estimated over the period 1995-2006. Panels (c), (d), (e), and (f) represent the seasonal evolution of the total precipitation over the same period from GPCP (blue, along with its associated error bar) and USW4 (red), averaged over the boxes indicated in Fig. 1 or over the whole domain.

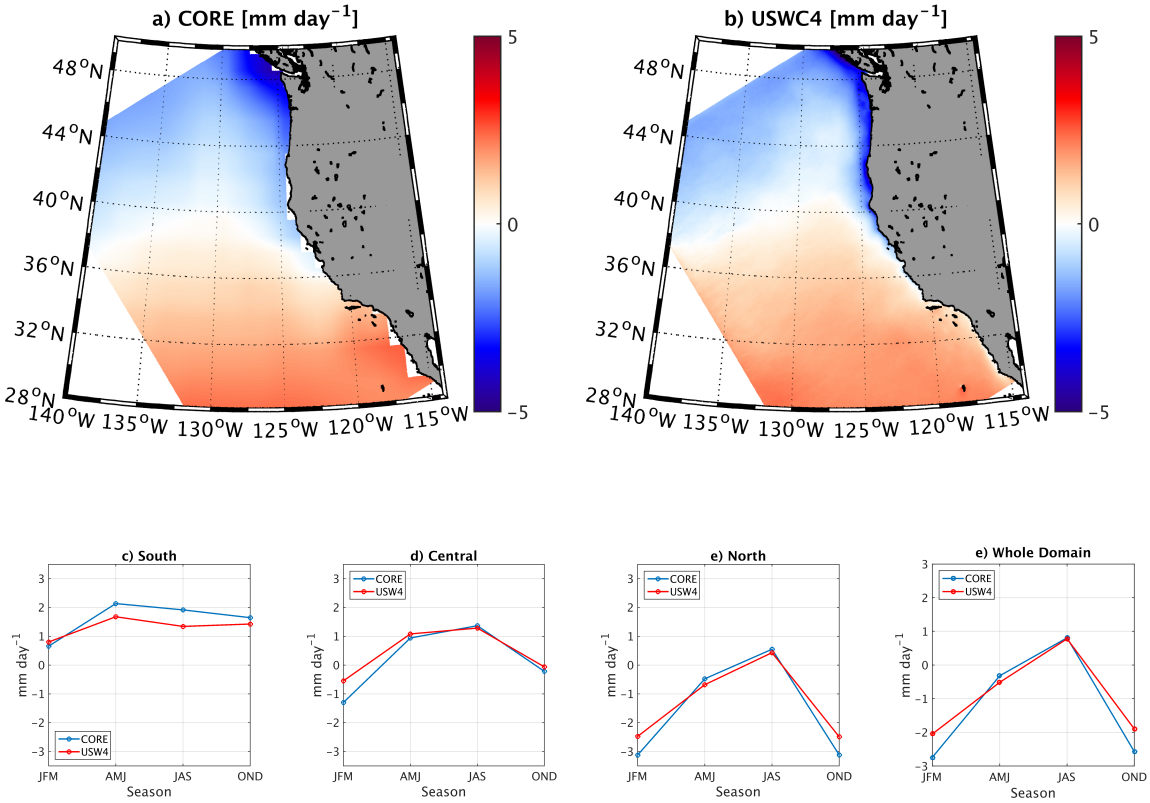


Figure 7: Net surface freshwater flux from (a) CORE and (b) USW4 over the period 1995-2006. Panels (c), (d), (e), and (f) represent the seasonal evolution of the net surface freshwater flux over the same period from CORE (blue) and USW4 (red), averaged over the boxes indicated in Fig. 1 or over the whole domain. The simulation reproduces the main spatial pattern of the observed freshwater flux and its seasonal variability.

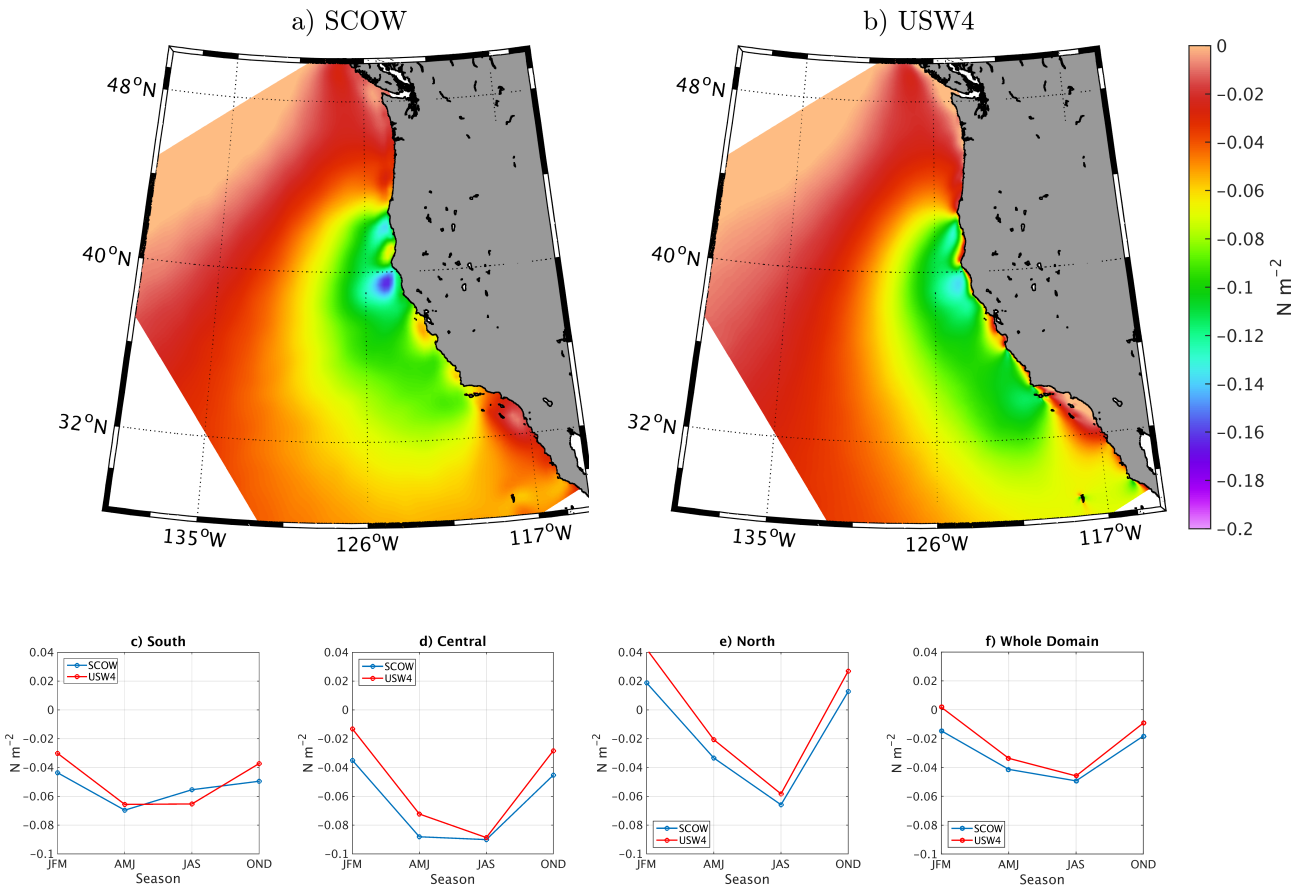


Figure 8: Mean meridional surface stress from (a) SCOW and (b) USW4 for the upwelling season (spring and summer) estimated over the period 2000-2009. Panels (c), (d), (e), and (f) represent the seasonal evolution over the same period from SCOW (blue) and USW4 (red), averaged over the boxes indicated in Fig. 1 or over the whole domain. USW4 reproduces the main surface stress spatial pattern and its seasonal evolution.

where the surface stress is weak compared to other parts of the CCS, and it is overestimated in USW4; perhaps the complicated small-island geometry is a contributing cause. Similar results are found using the QuikSCAT interannual product (Bentamy and Fillon, 2012).

# 4 Oceanic Fields

In this section the oceanic simulation is evaluated with respect to observations, and the oceanic impact of the synoptic wind variability is assessed.

## 4.1 Surface Layer

To evaluate the performance of the simulated oceanic simulation in terms of SST, we use the Ostia product as a comparison (Fig. 9), examining both Nearshore and Offshore boxes. In global coupled models, eastern boundary upwelling systems, such as the CCS, are characterized by large SST biases (up to 3°C; *e.g.,* Richter (2015)). The origin of these biases is not well understood, but it is likely to be caused by poor representations of the cloud cover, surface wind pattern, oceanic upwelling, and cross-shore eddy heat flux. In USW4 the mean SST large-scale patterns are qualitatively well represented compared to the SST satellite observations, with warmer waters to the west and south of the domain and colder waters to the north (Fig. 9) . The favorable upwelling season (*i.e.,* spring and summer) is captured by the simulation, and the upwelling signature is clearly marked in a 30 km wide coastal strip (Fig. 9). The simulated SST has a weak cold bias of 0.5°C over the whole domain in all the seasons, and the coastal water is colder in the model than in the Ostia product by up to 1°C (Figs. 9 and 10). Ostia SST has a relatively high spatial resolution of nominally 5 km. However, high cloud cover over the upwelling season impedes access to high-resolution data. Therefore, the effective resolution of this product may be similar to that of the microwave satellite products (25 km); this may partially explain the nearshore SST discrepancies between USW4 and the Ostia product. The largest bias is situated in the Southern California Bight where the atmospheric forcing is also less skillful (*i.e.,* overestimation of the surface stress and underestimation of the shortwave radiation during summer). Generally, numerical simulations have difficulty representing the southward extension of the cold water south of Pt. Conception. Oceanic simulations forced by climatological forcing do not simulate the southern coastal extension of the SST in a realistic way (Marchesiello et al., 2003; Capet et al., 2008a; Renault et al., 2016a) (Fig. 10), nor does the simulation reported by Veneziani et al. (2009) forced by the COAMPS atmospheric fields. USW4 has at least fair representation of this southward extension; *e.g.,* it has a better representation of the SST and of its mean pattern than a climatological solution (or the Veneziani et al. (2009) solution). In particular, in the Central Nearshore box, the climatological solution has a warm bias up to 1.5°C, whereas USW4 has a bias lower than 0.5°C there. Otherwise, the USW4 SST compares well with the observations, which is likely due to a good representation of the simulated atmospheric forcing (in particular, the cloud cover and wind drop-off) and of the surface currents.

Sea Surface Salinity (SSS) is higher offshore in the subtropical gyre with its high evaporation rate and is lower in the subpolar gyre with the higher precipitation. In addition, it decreases weakly near the coast, more so in the north, mainly due to river inflow. We compare the large-scale pattern and seasonal cycle of SSS from USW4 to those from the WOD13 SSS large-scale pattern

and seasonal cycle in Fig. 11. Due to a realistic representation of the freshwater flux by USW4 (Sec. 3c), there is good agreement between the simulation and the observations. However, offshore in central California, the SSS is generally too low with respect to the observations, with a maximum bias of 0.5 PSU. This is partially explained by the freshwater flux biases in Fig. 7, where the offshore flux is slightly underestimated. However, as discussed in Secs. 2.1 and 4.2, the bias is also partially inherited from the parent solution and its open boundary conditions. Near the Columbia River the USW4 SSS is conspicuously fresher than in WOD13, but the latter is probably horizontally overly smoothed.

In previous studies (*e.g.,* de Boyer Montégut et al. (2004)), the Mixed Layer Depth (MLD) definition can be based on different parameters such as temperature, salinity, and density. The MLD is typically defined using a threshold, for which the MLD is the depth at which potential temperature or potential density changes by a specified small value relative to its value near the surface. Here the CARS analysis definition is applied to the daily average temperature and density field in USW4. The MLD is defined using a temperature threshold of $\Delta\Theta = 0.2\ ^{\circ}$and $\Delta\sigma_{theta} = 0.3$ kg m$^{-3}$. The near-surface reference depth is $10$ m. MLD is shallower near the coast due to an uplifted pycnocline, and it is deeper in summer in the offshore subpolar gyre due to its depressed pycnocline compared to the offshore subpolar gyre with its uplifted pycnocline. The CARS MLD and the one estimated from USW4 are compared in Fig. 12. The phase and amplitude of the seasonal cycle are similar in both the model and observations: a shallowing of the MLD during spring and summer, then a deepening from 20 m to 80 m in winter. The MLD in the model is slightly too deep compared to climatology; this could be related to the surface forcing and to the KPP parameterization scheme (Large et al., 1994) for vertical mixing of tracers and momentum in ROMS. The vertical mixing that is too deep partially explains the cold bias in the simulated SST.

## 4.2 Interior $T$ and $S$

The CCS is stably stratified almost everywhere. It has warm temperature and fresh salinity in and above the pycnocline compared to below, and the pycnocline tilts upward toward the coast due to upwelling. Systematic large-scale hydrographic sampling of the CCS was initiated in 1949 by the California Cooperative Oceanic Fisheries Investigations (CalCOFI) program. Along the zonal line 80 of the CalCOFI data (offshore from Pt. Conception, centered on 33°N), the vertical structure of the simulated temperature, salinity, and density are in general agreement with the CalCOFI climatology (Fig. 13). The positive cross-shore slope of the isotherms, isohalines, and isopycnals are well reproduced. At the surface, consistent with Fig. 9, the mean SST is well reproduced due to a realistic representation of the net surface heat flux. As shown in Fig. 11, the mean salinity in the upper layer is too low with respect to CalCOFI (by 0.2 PSU). Finally, at depth, the mean density field is also realistic; nevertheless, there is a cold temperature bias (a negative density bias) that is partly compensated for by a fresh salinity bias (a positive density bias). Similar results are found for the Newport line using the WOD13 dataset (1955-2013, Fig. 14).

Figure 15 shows the mean temperature, salinity, and density biases at 150 m depth. In the first 500 km from the coast, the density is realistic with a very weak bias by less than 0.1 kg m$^{-3}$, and nearshore, where there is more data, the bias is less than 0.05 kg m$^{-3}$. However, consistent with Fig. 13, there is a bias compensation between the temperature and salinity. As suggested by Fig. 13, the temperature and salinity biases are mostly inherited from the open boundary conditions (*i.e.,* Mercator fields corrected by WOA) used in the parent-grid solution. Sensitivity tests have been

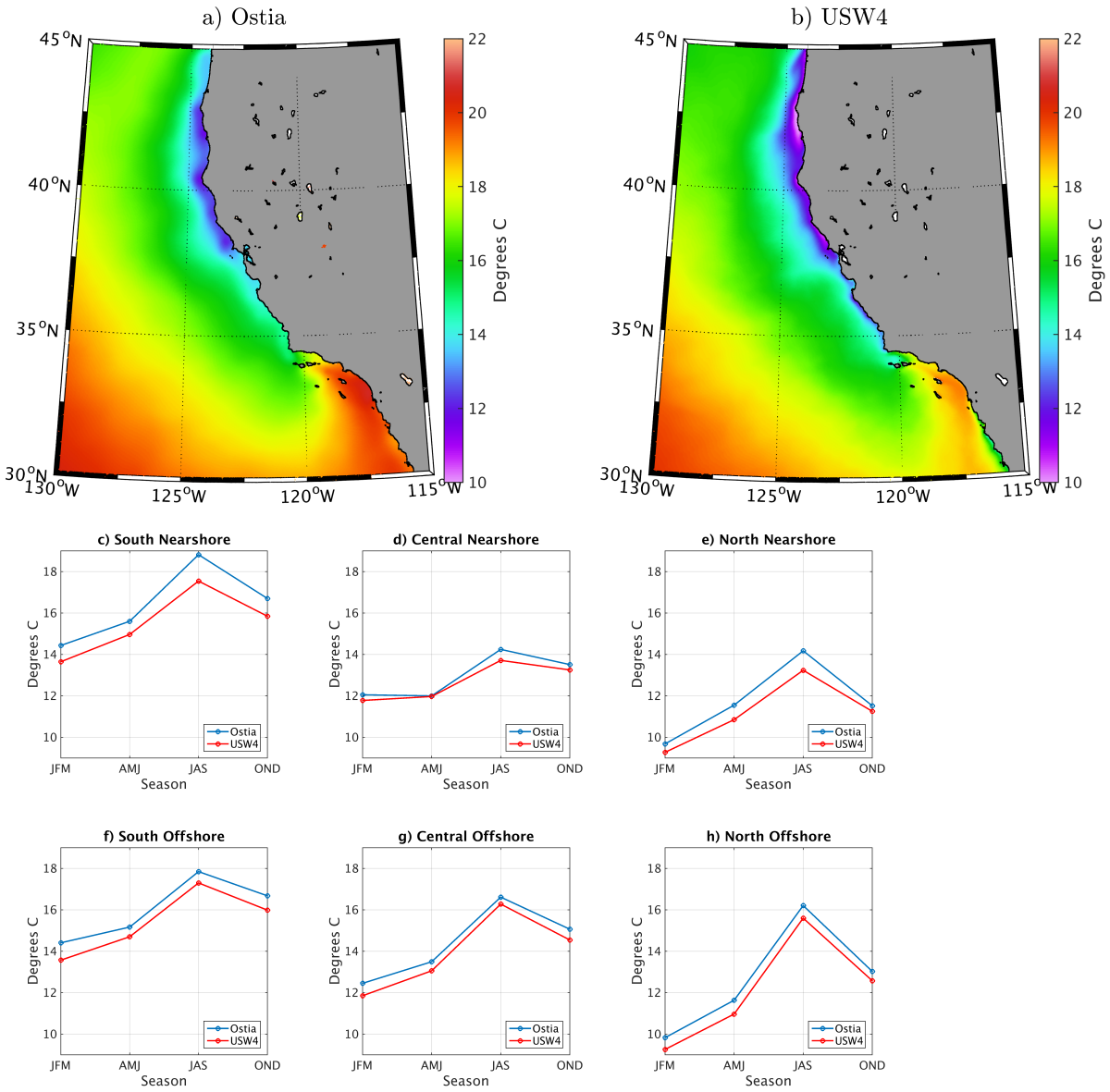


Figure 9: Mean SST [°C] during summer from (a) Ostia and (b) USW4 (1995-2010). Panels (c) to (h) represent the seasonal evolution of the SST over the same period from Ostia (blue) and USW4 (red) and averaged over the Nearshore and Offshore boxes indicated on Fig. 1 or over the whole domain. The SST patterns are well matched in USW4 with a mean negative bias lower than 0.5°C.

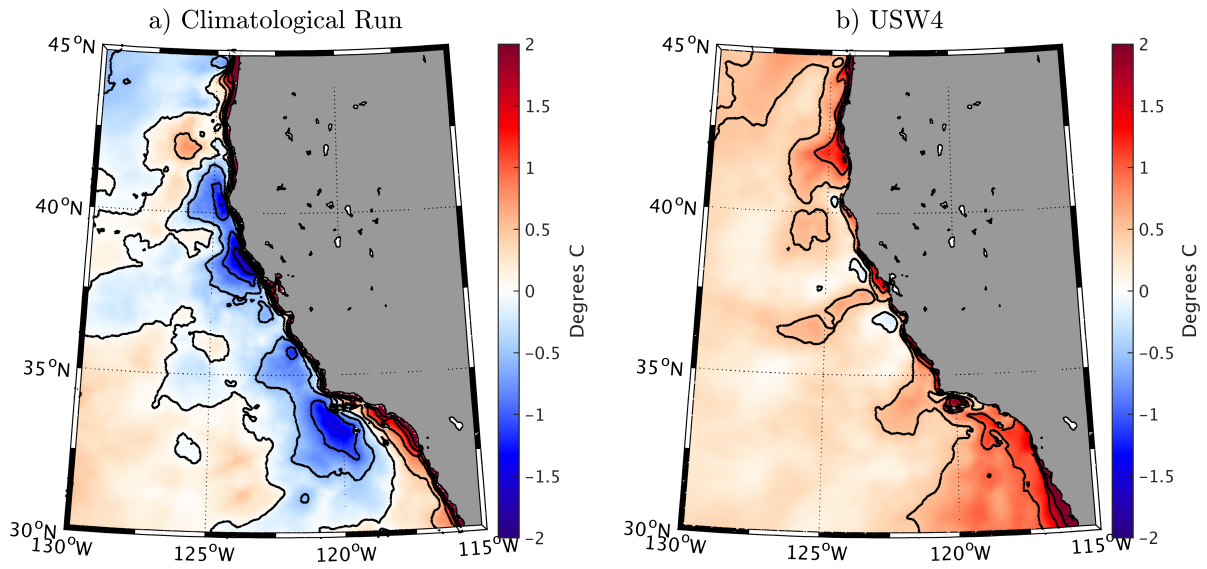


Figure 10: (a) Mean SST differences [°C] during summer between Ostia and (a) a climatological solution (*e.g.,* Capet et al. (2008b); Renault et al. (2016a)) and (b) USW4. USW4 has a cold bias ($< 0.5$ °), in particular over the Southern California Bight; however, it is less biased than the climatological solution (up to 2°C; see text in Sec. 4.1).

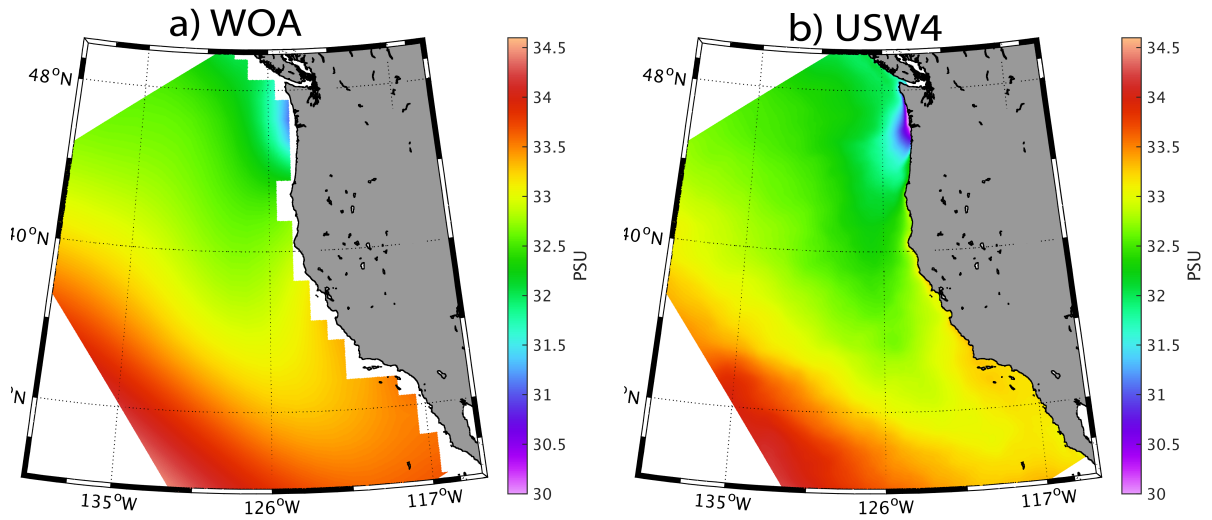


Figure 11: Mean SSS [PSU] prom (a) the World Ocean Atlas and (b) USW4 (1995-2010). Due to a realistic freshwater flux, the mean SSS is well represented by USW4 despite a small negative bias (up to 0.5 PSU).

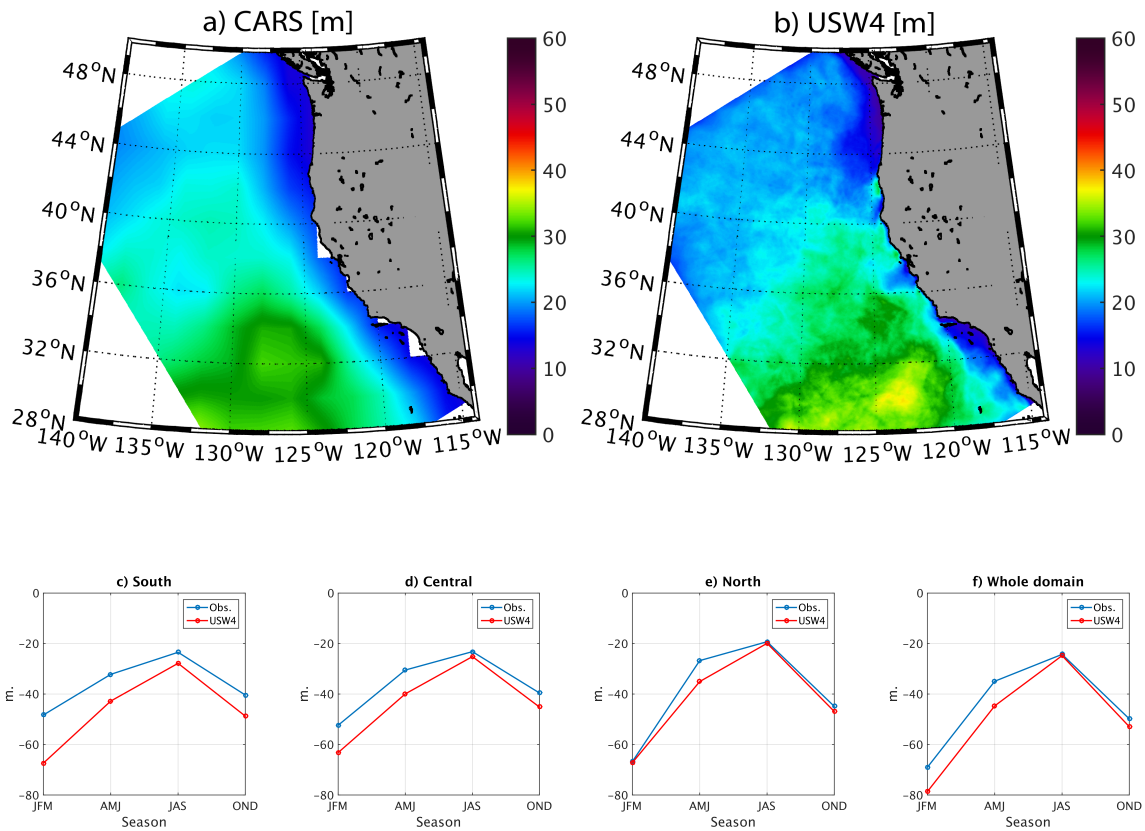


Figure 12: Mean Mixed Layer Depth (MLD) [m] estimated from (a) CARS and (b) USW4 during summer (1995-2010). Panels (c), (d), (e), and (f) represent the seasonal evolution of MLD over the same period from CARS (blue) and USW4 (red), averaged over the boxes indicated in Fig. 1 or over the whole domain. The simulation has a realistic MLD that is deeper farther offshore and during winter, but with a slight overestimated (up to 20 m in the Southern California Bight during winter) that partially explains the cold bias in SST in USW4.

made to reduce these biases. For example, more realistic results are obtained by using Mercator (compared to the Simple Oceanic Data Assimilation (SODA) by Carton and Giese (2008)) as the open boundary condition of the parent simulation and by correcting these data with WOA (not shown). In general, however, the sampling density of measurements in the offshore region is rather small, and we choose not to artificially diminish our large-scale biases by adjusting the boundary conditions within their (considerable) level of uncertainty. Deutsch et al. (2019a) discusses the importance of correctly reproducing the density field in specifying the biogeochemical boundary conditions.

The CCS has variability on many time scales: seasonal cycle, interannual variability (especially ENSO near the coast Jacox et al. (2015)), and mesoscale eddies. The temperature and salinity variability in USW4 is evaluated by comparing their standard deviations (removing the long-term mean) at $150$ m to the Word Ocean Database 2013 (WOD13, Fig. 16). In the nearshore region (first $200$ km from the coast), as in the observations, the upwelling signature on the water masses is well reproduced: there is a weaker temperature and salinity variability with respect to offshore. Offshore the $T$ and $S$ variability is mainly due to variations in the pycnocline depth in the subtropical gyres. In USW4 the offshore salinity variability is slightly too weak compared to the observations; while no doubt part of this discrepancy may be due to model bias (*e.g.,* inherited from the parent solution and boundary conditions), it could also partially be explained by uncertainties in the observations (*e.g.,* the salinity variability pattern in WOD13 is somewhat noisy). However, the offshore temperature variability is well reproduced by the model.

Finally, Fig. 17 shows the Potential Temperature - Salinity (TS) diagram as estimated from WOA and from USW4 between 30°-49°N in the upper 1000 m near the coastline (0-100 km offshore). The mean water masses of the CCS are well represented in USW4, although there are modest cold temperature and fresh salinity biases, consistent with Figs. 13-14.

## 4.3 Mean Sea Surface Height and Current

The mean Sea Surface Height (SSH) in the CCS is depressed at the coast due to the southward geostrophic current, and it further decreases poleward due to the equatorward wind stress. The SSH and the corresponding geostrophic current (Sec. 2c) from the 16 years of USW4 are shown in Figs. 18 and 19, along with observations from the $1/4°$resolution CNES-CLS13 dataset (Rio et al. (2014), Sec. 2d). The spatial distribution and amplitude of the simulated SSH is in good agreement with the observations. The main differences between the model and observations are located along the coast. Such discrepancies can be attributed partially to the Nearshore box width ($50$ km) which is unresolved in the satellite data (Ducet et al., 2000; Rio et al., 2014). The negative cross-shore SSH slope is well reproduced by USW4. Interestingly, the alongshore standing eddies are much less evident in USW4 and in the CNES-CLS13 dataset than in Centurioni et al. (2008) (drifter observations) or Marchesiello et al. (2003) (model), likely because of the longer time averaging used here.

The spatial pattern of the geostrophic current estimated from the observed and simulated SSH also compares well. The mean coastal current flows southward in both the observations and USW4 (Fig. 19), due to the mean southward wind stress (Fig. 8). The surface current is broad and generally equatorward, as observed (Swenson and Niiler, 1996). There is also an indirect validation of the simulated wind drop-off, as a poor representation of the slackening of the wind toward the coast may cause occasional surfacing of the California Undercurrent (CUC) through Sverdrup dy-

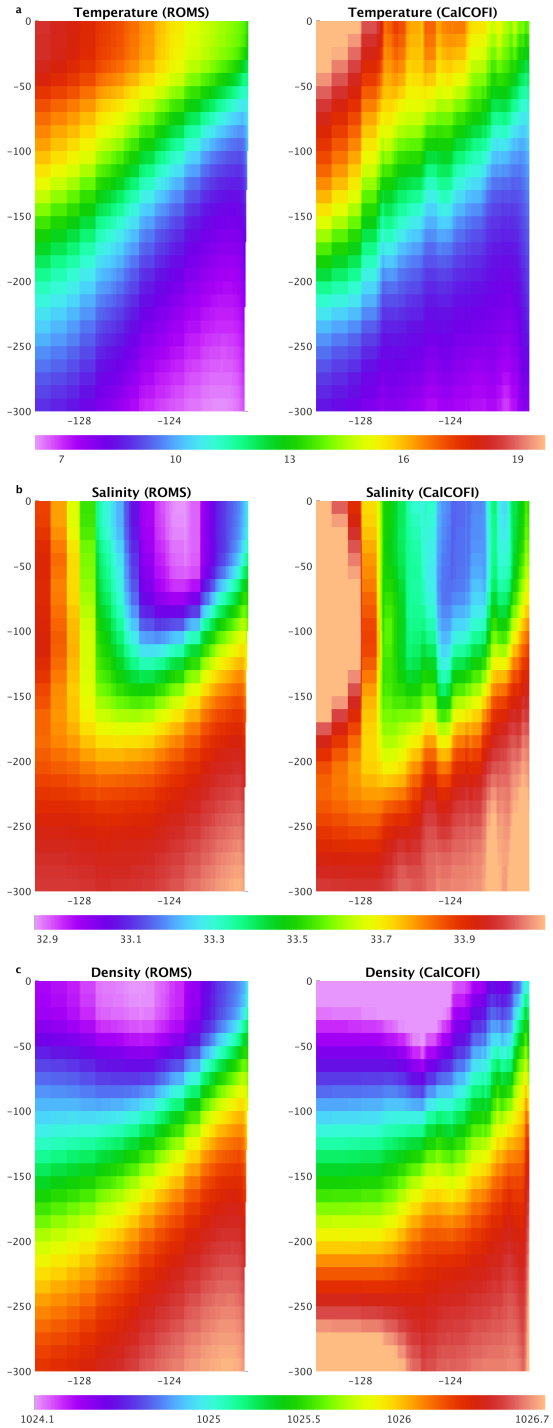


Figure 13: Mean cross-shore section along the CalCOFI line 80 ($\approx$ 33°N) of (a) temperature [°C], (b) salinity [PSU], and (c) density [kg m$^{-3}$] from USW4 (left column) and the CalCOFI observations (right). USW4 has approximately the right cross-shore density slope induced by the wind-driven upwelling. At the surface the salinity is too low with respect to CalCOFI. At depth the density is well reproduced, but there is a cold temperature bias (a positive density bias of $\approx$ 1°C), partially compensated for by a fresh salinity bias (a negative density bias) of $\approx$ 0.2 PSU).

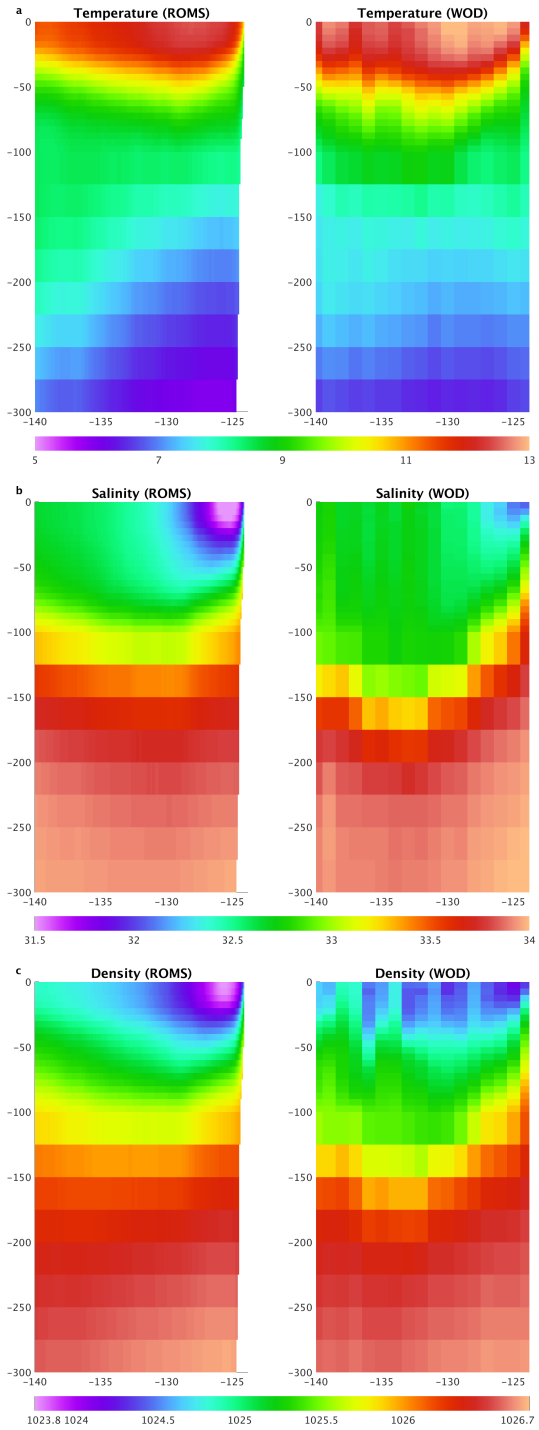


Figure 14: Mean cross-shore section along the Newport line ($\approx$ 45°N) of (a) temperature [°C], (b) salinity [PSU], and (c) density [kg m$^{-3}$] estimated from USW4 (1995-2010) and the WOD13 dataset (over the period 1955-2013). Similar results are found in Fig. 13.

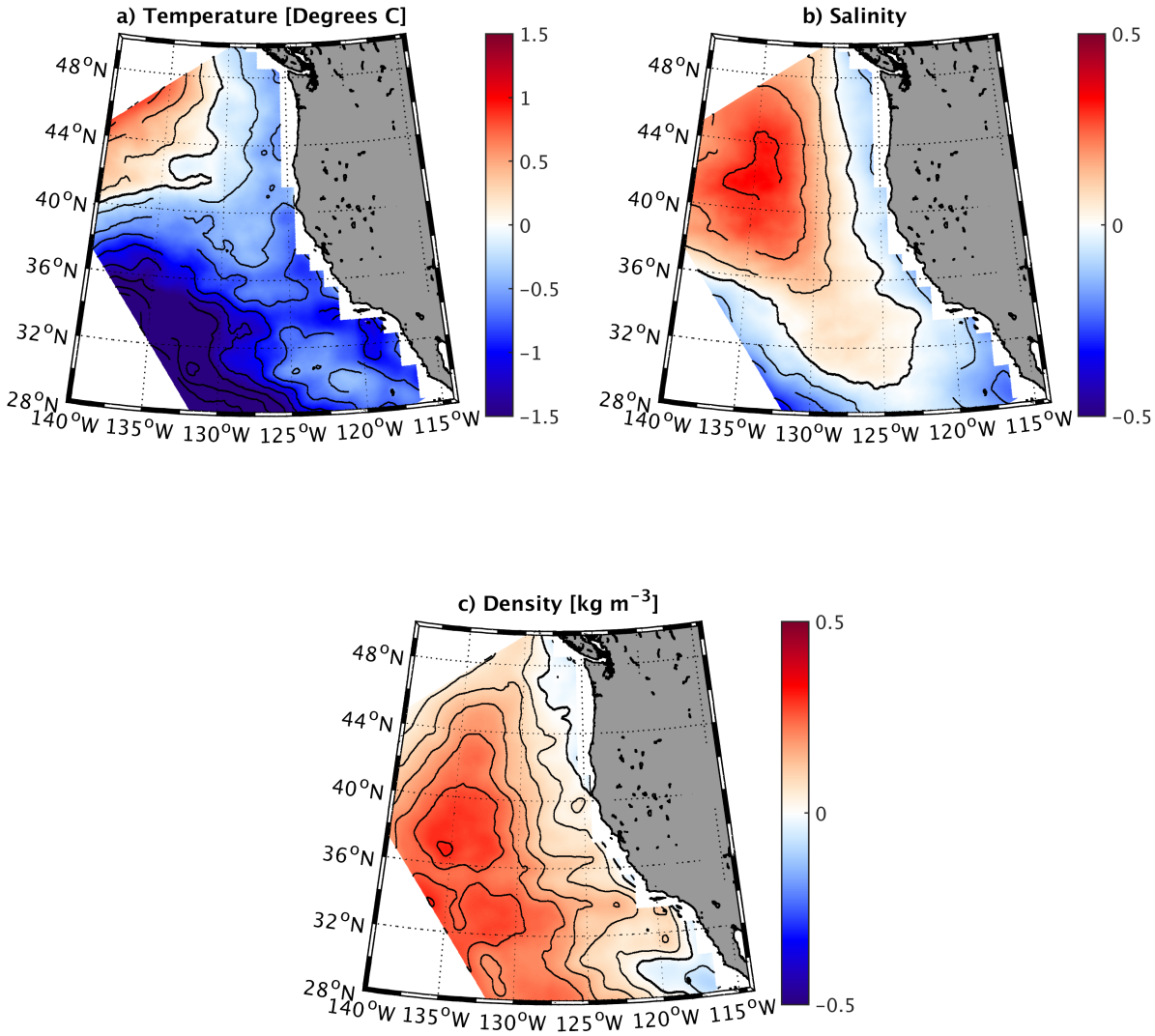


Figure 15: Mean temperature [°C], salinity [PSU], and density [kg m$^{-3}$] differences at 150 m depth between USW4 (1995-2010) and World Ocean Database 2013 (WOD13). The contour lines difference isolines, with the thick black line indicating zero difference. In the first 500 km the density at 150 m is realistic, with a very weak bias of less than 0.1 kg m$^{-3}$; nearshore, where there is more data, the bias is less than 0.05 kg m$^{-3}$. However, consistent with Fig. 13, there is a compensation between temperature and salinity biases. Most of the salinity bias enters the domain through the northern open boundary condition.

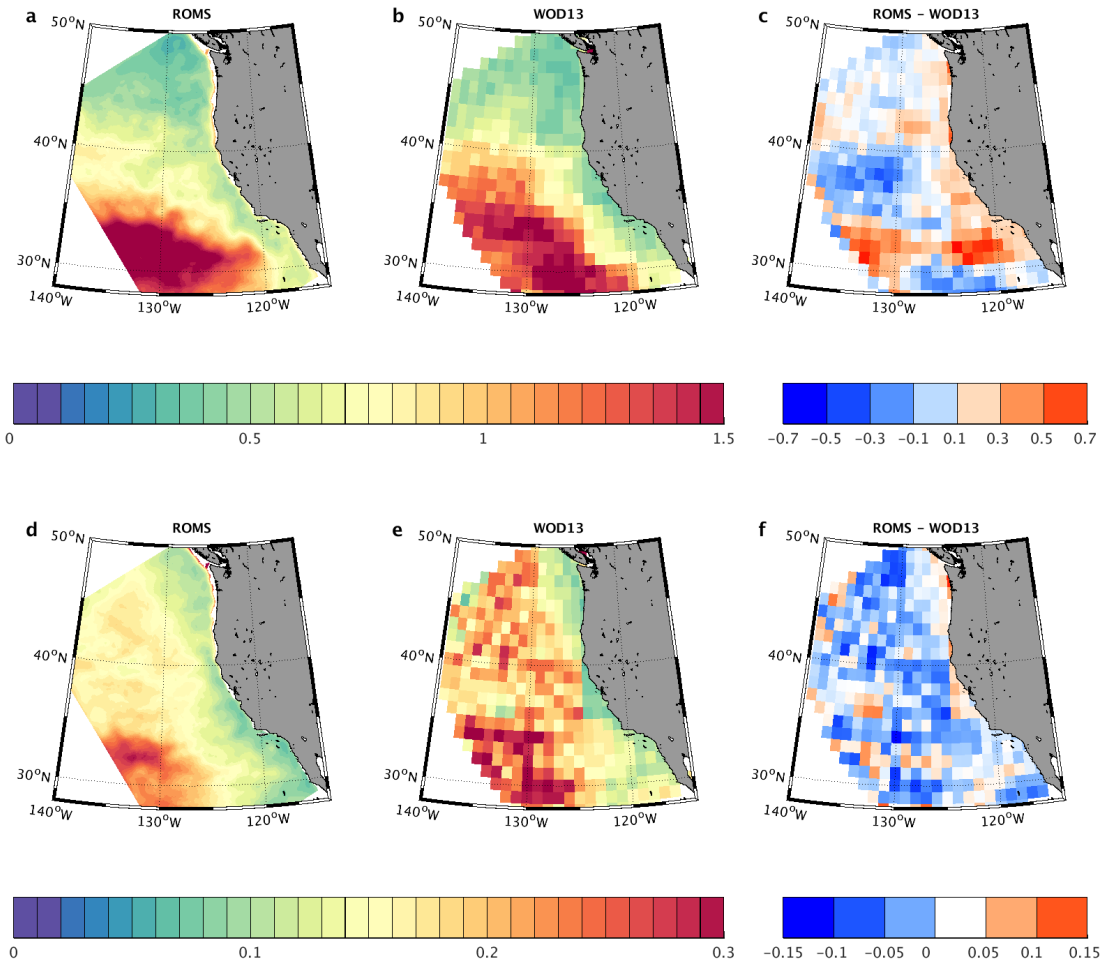


Figure 16: Top panel: Temporal standard deviation of temperature [°C] at 150 m depth for (a) USW4 and (b) World Ocean Database 2013 (WOD13). (c) The difference between USW4 and WOD13. Bottom panel: same as the top panel but for the salinity [PSU]. There is a general agreement between the simulated temperature and salinity variability at 150 m depth and the observations.

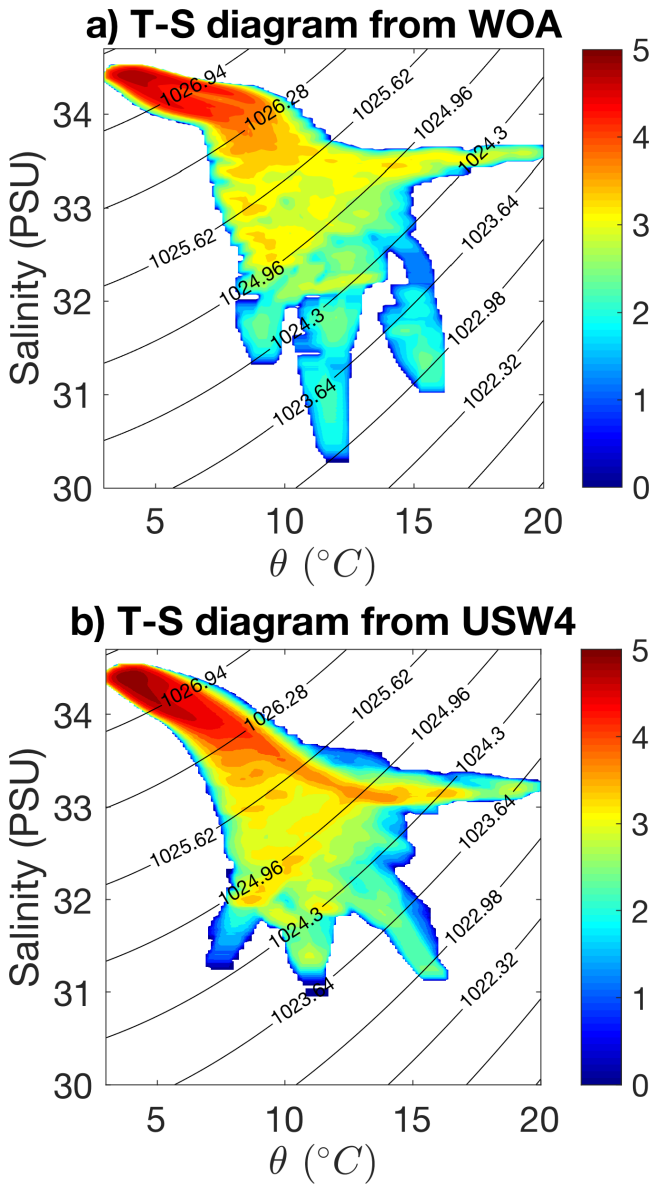


Figure 17: Potential Temperature - Salinity (TS) diagram from (a) the WOA observations and (b) USW4, for the climatological mean between 30°-49°in the upper 1000 m near the coast (0-100 km offshore). The colorbar shows the number of data points in each (1°C, 0.1PSU) bin on the logarithmic scale, and black contour lines are those of density. The abscissa is potential temperature with the surface as the reference level, and the ordinate is salinity. To obtain the number of data points in each bin, we first obtain the (T,S) dataset in each season, averaged over the years 1995-2010, in the selected region at a spatial resolution of 4 km in the off-shore direction, 0.05°($\approx$ 5 km) in the along-shore direction, and 20 m in the vertical direction; then, the number of data points in each bin is counted.

namics: a positive surface stress curl produces a barotropic poleward flow that adds to the coastal baroclinic flow (McCreary and Chao, 1985; Lynn and Simpson, 1990; Marchesiello et al., 2003). The maximum amplitude of the current is situated along the coast and, in the south, also offshore. It is slightly stronger in the model than in the observations; however, altimetric geostrophic velocity amplitude of the CNES-CLS13 dataset is often too weak, compared to *in situ* geostrophic velocities (Rio et al., 2013), because of its limited spatial resolution.

Figure 20 depicts coastal cross-shore sections of the mean alongshore current and vertical velocity averaged between 35°N and 40°N for winter, spring, summer, and fall. The current structure and the vertical velocities are in general agreement with the literature (*e.g.,* Marchesiello et al. (2003); Veneziani et al. (2009)). The model reproduces the onset of the upwelling from winter to spring. Between 35°N and 40°N, the upwelling is stronger during spring and is characterized by mean vertical velocities up to $4$ m day$^{-1}$. As reported in the observations, the coastal California Current System during the upwelling season is characterized by an equatorward surface current with a mean velocity of 0.2 m s$^{-1}$ overlying the CUC.

The CUC, one of the major components of the CCS, is a poleward flow in the upper hundreds of meters near the U.S. West Coast. It transports warm and salty equatorial equator poleward and plays a significant role in the local heat, salt and biogeochemical budgets. Quite a few studies exist characterizing the features and exploring the dynamics of the CUC (*e.g.,* McCreary et al. (1987); Lynn and Simpson (1987); Pierce et al. (2000); Gay and Chereskin (2009); Molemaker et al. (2015)). Figure 20 depicts coastal cross-shore sections of the mean alongshore current and vertical velocity averaged between 35°N and 40°N for winter, spring, summer, and fall. The current structure and the vertical velocities are in general agreement with the literature (*e.g.,* Marchesiello et al. (2003); Veneziani et al. (2009)). The model reproduces the onset of the upwelling from winter to spring. Between 35°N and 40°N, the upwelling is strongest during spring with a mean vertical velocity up to $4$ m day$^{-1}$. As reported in the observations, the coastal CCS during the upwelling season is characterized by an equatorward surface current with a mean velocity of 0.2 m s$^{-1}$ overlying the CUC.

To further assess the realism of the USW4 CUC, we characterize the mean CUC core properties from the 16-year average. At each cross-section, the location of the CUC core is defined as the location where the along-shore velocity reaches a positive maximum value within 60 km offshore and between 50 m and 500 m depth. This criteria is based on the CUC structures from both the USW4 solution and previous literature. After identifying the CUC location, we then obtain the alongshore velocity and potential density (with the surface as the reference level) at the CUC core. Using this approach, we evaluated all the cross-sections as a function of depth and offshore distance at all the latitudes ranging from 3°N to 49°N at a resolution of 0.05°(note similar results are found using a resolution of 0.1°, 0.2°, or 0.2°). A robust CUC is identified in all the latitudes. The core properties exhibit strong latitudinal variability (not shown). Figure 21 shows the histogram of the offshore distance, depth, potential density and along-shore velocity of CUC core based on a 16-year average. The core depth peaks at $100$ m, and the core density peaks at $1026$kg m$^{-3}$. The histogram of alongshore velocity indicates that the value is mostly smaller than $10$ cm s$^{-1}$. The histogram of the offshore distance is rather level with no distinct peak. The simulated CUC core properties qualitatively agree with previous studies, indicating that the USW4 solution can be a reasonable tool for future explorations of the dynamics and consequences of CUC. The offshore distance of the simulated CUC core ranges from $0$ to $60$ km with a mean value of $21$ km, roughly consistent with reported observational values of $10 - 50$ km (Gay and Chereskin, 2009). The

observed CUC core occurs near the density of $1026.4 - 1026.6$ kg m$^{-3}$ (Lynn and Simpson, 1987; Gay and Chereskin, 2009). Consistently, the range of potential density of the CUC core is narrow, from $1025.3$ to $1026.7$ kg m$^{-3}$, with a mean of $1025.9$ kg m$^{-3}$. The core velocity in the model has the same order of magnitude as the observed values summarized by Gay and Chereskin (2009): it ranges from $0.02$ to $0.2$ m s$^{-1}$, with a mean of $0.1$ m s$^{-1}$. Note the peak value is higher in a higher-resolution simulation (Molemaker et al., 2015). While previous studies suggest that the core depth is from $100$ to $300$ m (Chelton, 1984; Collins et al., 2003; Gay and Chereskin, 2009), the simulated core depth is slightly shallower: the mean depth is $103$ m and its range is $50 - 258$ m. Note that besides model bias, the fact that our results are based on the climate-mean state and cover the entire latitude range from 30°N to 49°N may contribute to the slight difference between model results and sparse observations.

As shown in Fig. 21, the typical values of CUC properties from the climate mean state of the USW4 solution agree well with previous literature. On the other hand, previous studies indicate that the CUC also undergoes significant temporal variability over a wide range of temporal scales (*e.g.,* semi-annual, seasonal, interannual and long-term trend (Bograd et al., 2003; Gay and Chereskin, 2009; Meinvielle and Johnson, 2013; Gómez-Valdivia et al., 2017)). In particular, the CUC exhibits a strong seasonal cycle (Lynn and Simpson, 1987; Collins et al., 2003; Gay and Chereskin, 2009). To estimate the temporal variability of CUC properties, we identify the core of the CUC for each season of each year over the period 1995-2010 using a similar approach as that for Fig. 21. The focus is over the central California region between 34.4°N - 42.8°N, *i.e.,* where the CUC is the stronger. The along-shore velocity is first estimated and averaged over 3-months periods and along the along-shore direction between 34.4°N - 42.8°N, and then the CUC core main properties are determined. Figure 22 depicts the seasonal cycle of the CUC core properties. The simulated CUC is characterized by a pronounced seasonal cycle with a shallower (deeper) core during winter and fall (spring and summer). Because the temperature decreases with depth, and salinity and density increase with depth, the core temperature of the CUC is relatively cold, and the salinity and density are relatively large in the spring and summer. The along-shore velocity of the CUC core reaches its maximum and minimum values during summer and winter, respectively. This is consistent with the float observations from Collins et al. (2004). The seasonal cycle of CUC transport is consistent with that of the along-shore velocity of the CUC core. A significant interannual variability of CUC properties occurs in the USW4 solution (see Fig. 23 where the seasonal cycle is removed). During the ENSO in 1997-1998, the CUC transport becomes very weak, and the CUC core is shallower after 2002. Finally, the good representation of the coastal current structure is also an indirect validation of the simulated wind drop-off. A simulation forced by the coarsely resolved NCEP reanalysis winds (NCEP2 or CFSR) leads to a surfacing of the CUC (not shown). Global atmospheric reanalyses, also due to their coarse resolution (*e.g.,* 40 km for CFSR), have too wide a wind drop-off that forces an excessive surfacing of the CUC and a poor representation of the EKE (Renault et al., 2016a).

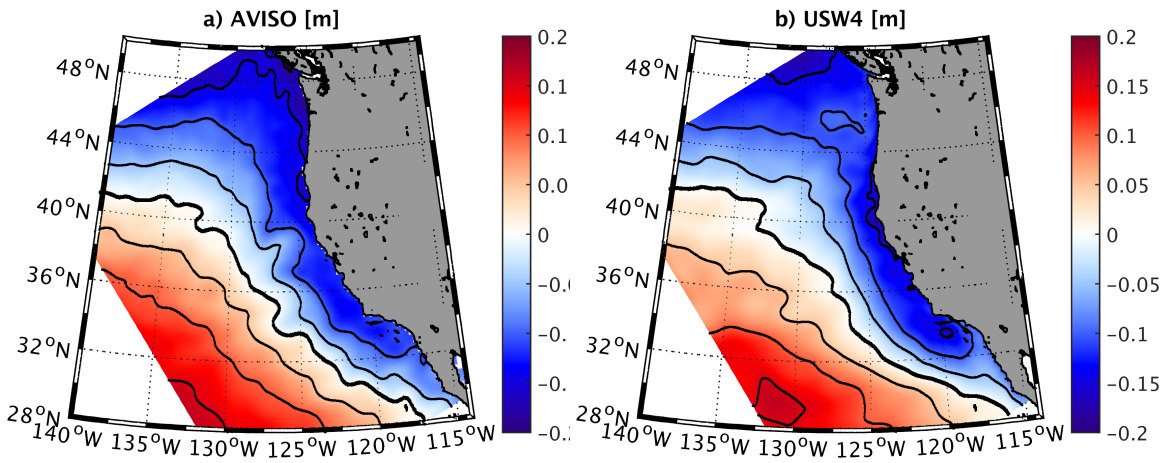


Figure 18: Mean Sea Surface Height (SSH) [m] from (a) AVISO and (b) USW4 over the period 1995-2010. Contours show 0.05 m increments of SSH, and the thick black line represents the local zero reference height contour. The simulation reproduces the mean SSH and its offshore gradient rather well.

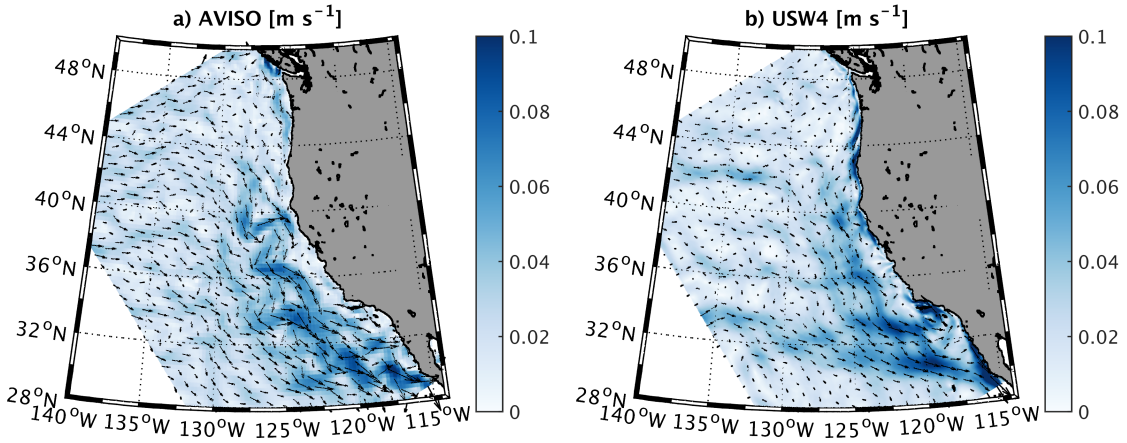


Figure 19: Mean surface geostrophic currents estimated from (a) AVISO and (b) USW4. The arrows give the direction, and the colors are the intensity. USW4 currents are in broad agreement with the observations given the estimation uncertainty for point values in both data sets. They represent the surface CCS southward flow, which is also an indirect validation of the surface stress cross-shore profiles (Sec. 4.3).

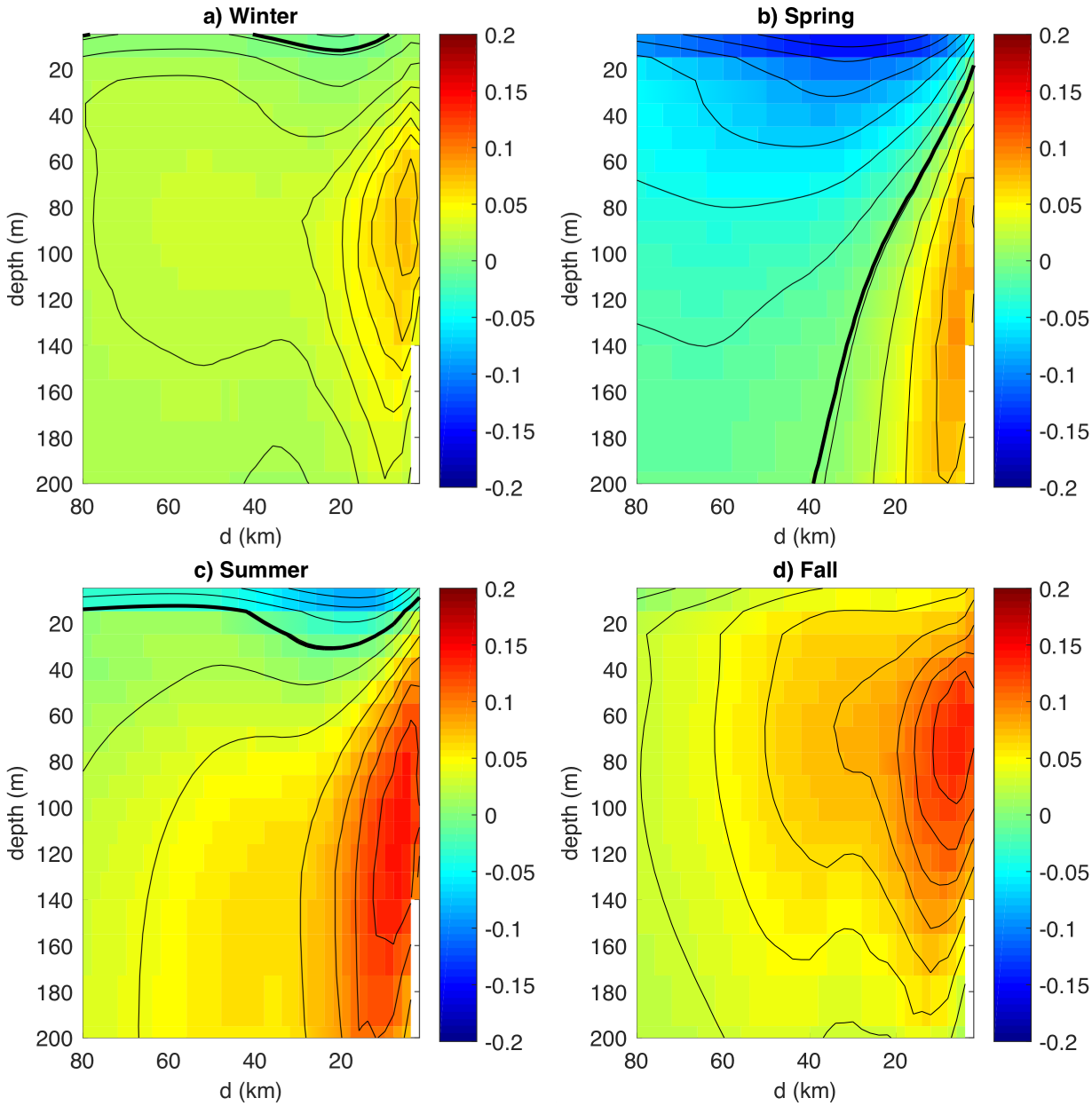


Figure 20: Cross-section of the alongshore current (colors) and vertical velocity (thick black lines with contours of 1, 2, and 4 m day$^{-1}$), averaged between 35°N and 40°N during spring and summer. The current structure shows a broad surface southward current and the CUC underneath against the upper continental slope. During summer the CUC shallows due to a larger wind curl, the mean vertical velocity is stronger, and the cross-shore isotherms have a larger slope due to upwelling of cold subsurface water.

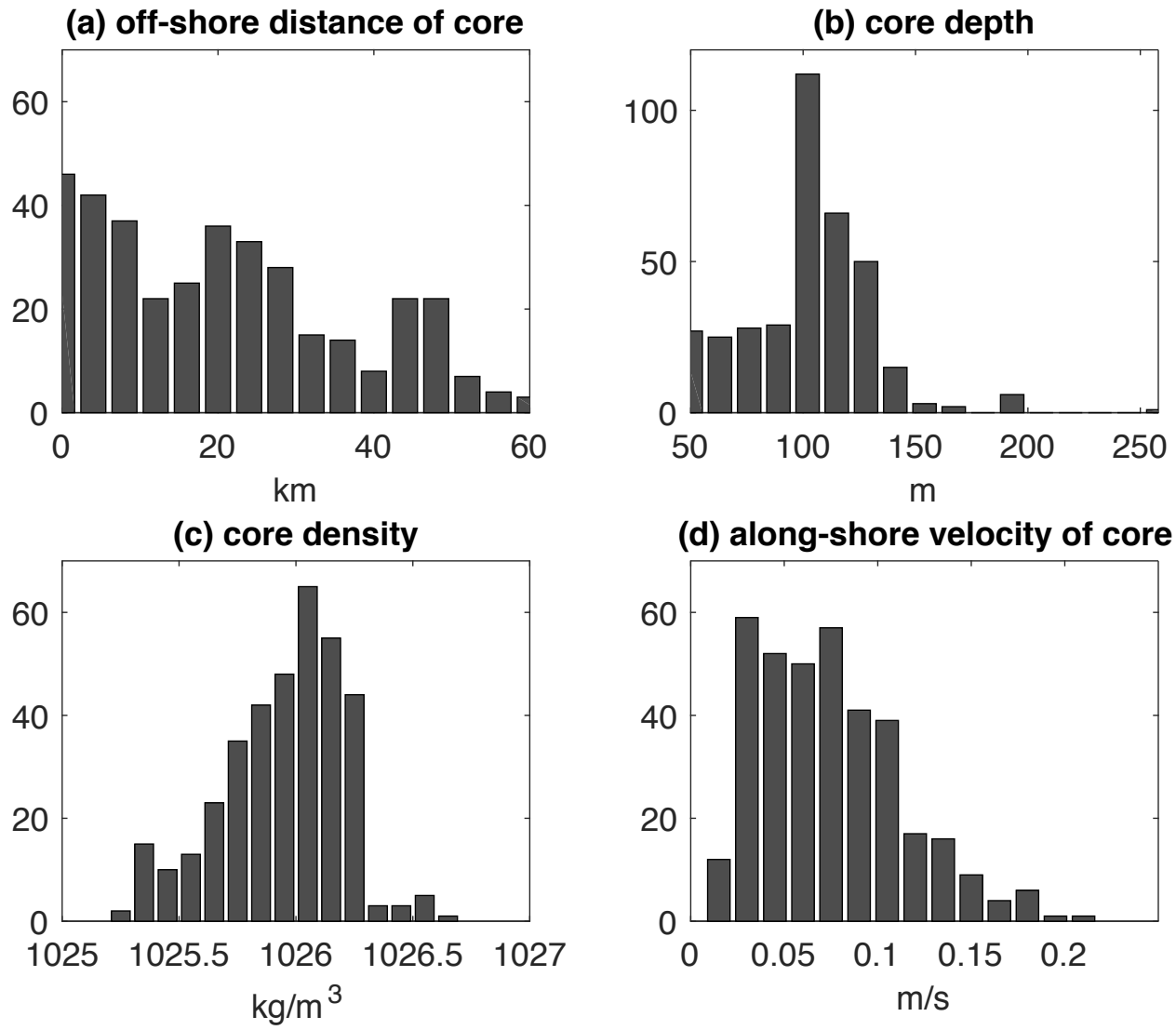


Figure 21: Histograms of (a) off-shore distance [km], (b) depth [m], (c) potential density [kg $m^{-3}$] and (d) along-shore velocity [m/s] for the core of the CUC between 30°N and 49°N with an alongshore resolution of 0.05°between offshore sections. The histograms in (a)-(d) are sorted into bins with sizes of 4, 13, 0.1, and 0.015 in their respective units.

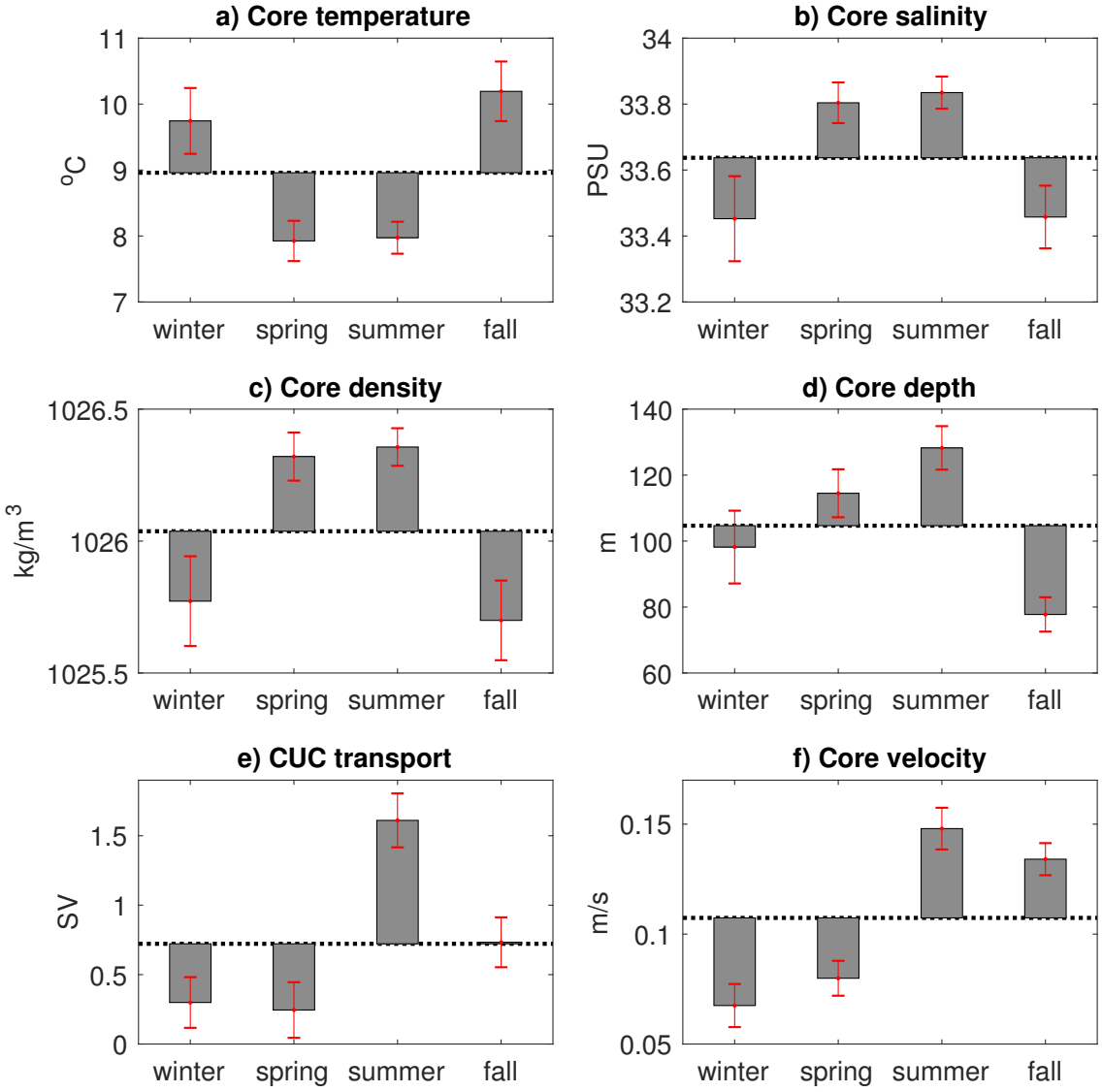


Figure 22: Seasonal cycle of the CUC core properties averaged between 34.4°N and 42.8°N as estimated from USW4 over the period 1995-2010. (a) Potential temperature of the core [°C], (b) salinity [PSU], (c) potential density [kg m$^{-3}$], (d) depth of the core [m], (e) transport [Sv], and (f) alongshore velocity [m s$^{-1}$]. The error bar (red) represents the 95% confidence level and has been estimated using the formula $2\sigma/\sqrt{N}$ applied to 3-month temporal averages following Chen et al. (2014), where $\sigma$ represents the standard deviation and N the number of degrees of freedom. The horizontal black dashed line denotes the time-mean value over the four seasons.

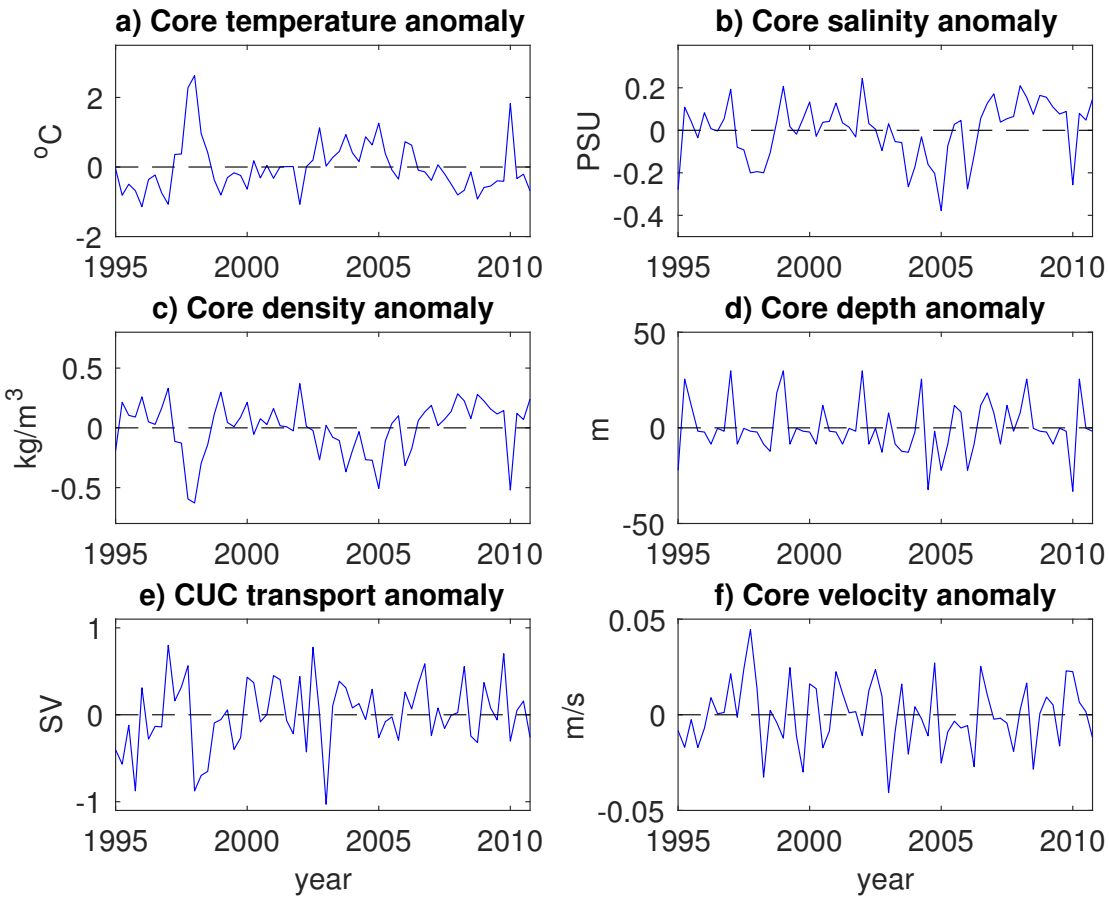


Figure 23: Seasonal anomalies of CUC core properties averaged between 34.4°N and 42.8°N as estimated from USW4 over the period 1995-2010. (a) Potential temperature of the core [°C], (b) salinity [PSU], (c) potential density [kg m$^{-3}$], (d) depth of the core [m], (e) transport [Sv], and (f) alongshore velocity [m s$^{-1}$].

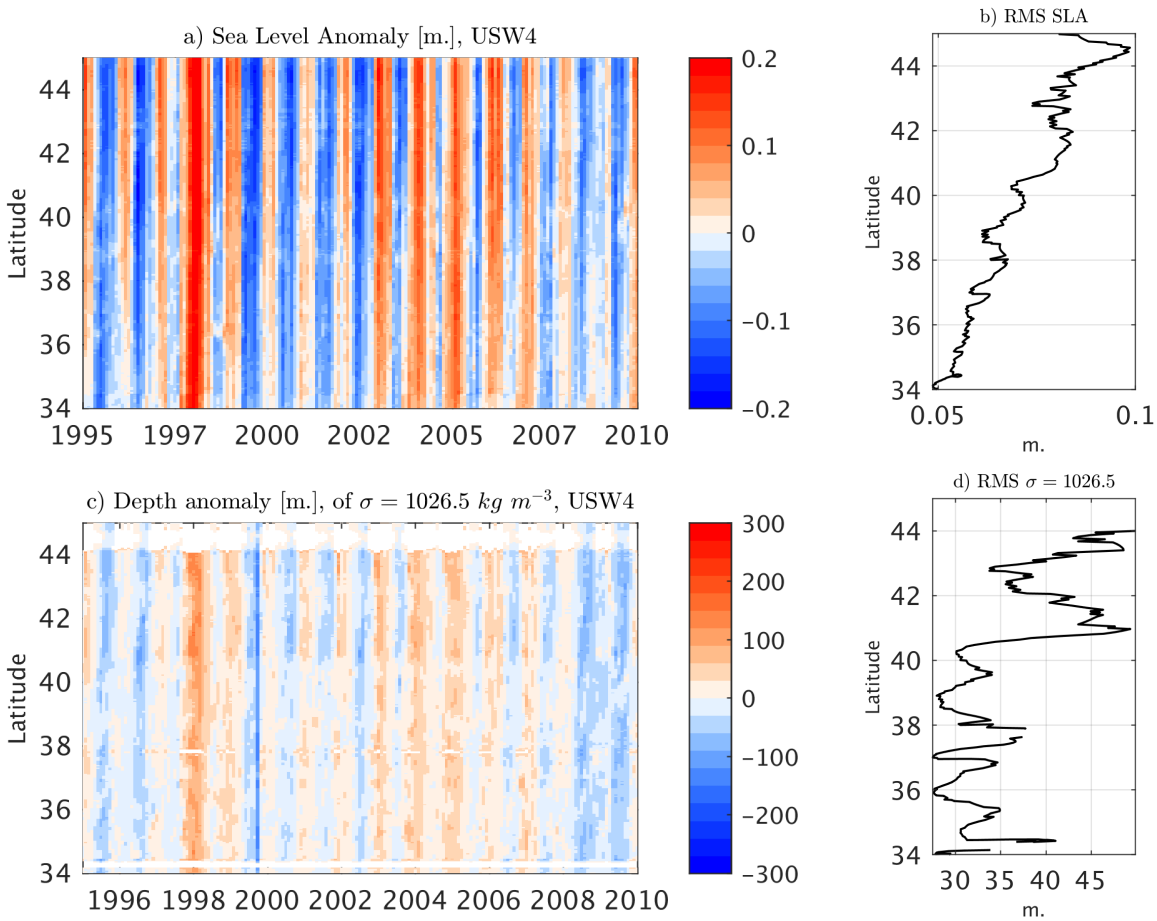


Figure 24: Hovmoller diagrams (latitude and time) for (a) SLA [m] and (b) depth of the $\sigma_\theta = 25.6$ isopycnal surface [m] at a distance $\approx$ 50 km offshore. On the right of each plot is the corresponding RMS latitude profile with respect to the temporal variability.

## 4.4 Low-Frequency Variability

The CCS exhibits broad-band variability. On time and space scales larger than the mesoscale, most of the variability is partly extrinsic to the region, reflecting the larger-scale seasonal, interannual, and decadal climate signals that have regional manifestations along the U.S. West Coast (Chhak and DiLorenzo, 2007; Lorenzo et al., 2009; Chenillat et al., 2012; Meinvielle and Johnson, 2013; Davis and DiLornezo, 2015).

To give a sense of this variability, Fig. 24 shows the whole-coast history of the sea-surface height (SLA) and depth of a pycnocline isopycnal over the reanalysis period. The along-coast coherence of SLA is striking, as is the regularity of its primarily seasonal oscillation. Its amplitude increases to the north because the amplitude of the seasonal cycle of the alongshore wind and current increase as well. A rapid poleward propagation speed $\approx 2.5$ m s$^{-1}$ is apparent on average, as has been extensively analyzed previously (Chelton, 1984; Spillane et al., 1987). The interannual variability amplitude is a modest fraction of the seasonal one, most of the time, but the 1997-98 ENSO event is particularly prominent (Kosro, 2002; Ryan and Noble, 2002; Lynn and Bograd, 2002).

The pattern in pycnocline depth is somewhat more complex, although the temporal correlation with SLA is evident ($C \approx 0.8$, more or less uniformly along the coast). The amplitudes of both quantities have an increasing trend to the north, but the depth anomaly exhibits more modulation in amplitude than the SLA with moderate drops at particular latitudes that are related to interruptions in the path of the CUC along the coast (Chen et al., 2019).

## 4.5 Mesoscale Activity

The mean CCS circulation is unstable and generates mesoscale eddies primarily by baroclinic instability (Strub and James, 2000; Marchesiello et al., 2003); as a result there is a peak in the EKE distribution a couple of hundred km away from the coast. The EKE has a moderate seasonal cycle with largest values during summer and fall following the seasonal peaks in the surface stress (Fig. 8). The geostrophic surface EKE is estimated over the period 1995-2010 from AVISO (Ducet et al., 2000) and from USW4. For the model the EKE is computed using low-pass filtered geostrophic velocities with a Gaussian spatial filter with a 36-km half-width as an approximation to AVISO's resolution (Chelton and Schlax, 2003). (More precise comparisons could be made using simulation fields processed in the same way as altimetric observations.) The simulated EKE has its largest values not too far offshore and exhibits a wide decay zone further offshore (Fig. 25). This pattern is due to the combined influences of Ekman transport, eddy dispersion, and the eddy killing effect of the current feedback, with an overall similarity to AVISO and the literature (*e.g.,* Capet et al. (2008a)). The overall EKE amplitude is about right in USW4, but there are some biases in the USW4 spatial pattern, mainly that the EKE is too large in the near-coastal region, and the EKE is too large in the Southern California Bight, which seems most likely due to errors in the atmospheric forcing. Part of the discrepancy may be due to model bias, *e.g.,* the current feedback induces a dampening of the mesoscale activity, but the wind response induces a partial re-energization. In USW4, following Renault et al. (2016d), the $s_w$ coefficient is used to mimic the wind response to the current feedback. However, it is taken as spatially and temporally constant, which could induce, for example, a re-energization that is too strong in the nearshore region. However, in the nearshore region in particular, this could also be partially explained by uncertain-

ties in the observations. Figure 25 shows the seasonal cycle of the EKE as estimated from the observations and from the USW4 low-pass filtered geostrophic velocities with a Gaussian spatial filter with 36-km half-width (solid line) and 28-km-half-width (dashed line). USW4 realistically simulates the seasonal evolution of the EKE, with larger EKE values in summer and spring.

The relevant EKE conversion rates (Sec. 2c) in USW4 are evaluated over the period 1995-2010 (Fig. 26a), and a mean cross-shore profile between 30°N and 45°N is estimated for each term (Fig. 26b). The geostrophic eddy wind-work $F_eK_{eg}$ profile is also estimated using a QuikSCAT product (Bentamy and Fillon, 2012) and AVISO, but only over the available QuikSCAT period (2000-2009). (Due to the QuikSCAT and AVISO coastal accuracy issues, the $F_eK_{eg}$ value over the first 50 km off the coast is not shown.) Consistent with Marchesiello et al. (2003) and Renault et al. (2016d), the main sources of EKE are the eddy wind-work and the baroclinic conversion. Both have large positive values in the nearshore region. The $K_mK_e$ conversion is a secondary term. Consistent with the observations, $F_eK_{eg}$ is positive in the nearshore region and then becomes negative offshore, deflecting energy from the oceanic geostrophic eddy currents to the atmosphere and thus dampening the offshore eddies. USW4 deflects slightly more energy offshore than the observations (by 10% averaged over the offshore area). This could be due to estimation errors in the observations, but it might also be due to biases in the atmospheric and oceanic simulations, with an overestimation of the EKE reservoir (more energy to be deflected) and a biased estimation of $s_w$ when estimating the surface stress. For example, $s_w$ has a seasonal cycle (Renault et al., 2017) and depends on the atmospheric parameterization of the marine boundary layer (Renault et al., 2016d), and these dependencies are not included in these reanalysis simulations. This may explain the slight overestimation of the offshore EKE and the overestimation of the eddy life in EXP3 shown by Renault et al. (2016d). Overall, however, the parameterization of the wind response to the current feedback in USW4 reproduces the observed EKE and $F_eK_{eg}$.

## 4.6 High-Frequency Wind Forcing

In a bulk formula the surface stress has a quadratic dependence on the wind. As a result, time-varying winds contribute to the time-mean surface stress. It is well known that neglecting high-frequency winds can induce large errors in the surface stress estimate (Esbensen and Kushnir, 1981; Gulev, 1994; Wu et al., 2016). Recent studies show those errors can cause large biases in kinetic energy transfer between the atmosphere and ocean (Zhai et al., 2012; Zhai, 2013). In particular, Zhai et al. (2012) using a global ocean model shows the mean wind-work increases by 70% when using a 6-hourly wind update instead of a monthly one. A few previous studies assess the role of high-frequency atmospheric wind in determining the ocean circulation. They find that it can lead to an increase by about 50% in both the mean wind-work and the EKE, as well as a strengthening of the wind-driven subtropical gyre by about 10-15% (Holdsworth and Myers, 2015; Wu et al., 2016; Condron and Renfrew, 2013).

To determine the importance of high-frequency wind forcing in the CCS, three additional experiments have been carried out for the period 1995-1999 using a 6-hourly-averaged wind forcing (6H), a daily-averaged wind forcing (1D), and a monthly-averaged wind forcing (1M). The mean alongshore surface stress and the EKE averaged along a coastal band 100 km wide are illustrated in Fig. 27 and summarized in Table 1. From a 1-hourly (*i.e.,* USW4) to 6-hourly wind forcing, the surface stress is only slightly impacted by 3%. When estimating the stress using 1D, it is slightly underestimated by 6%. This is, for example, the error made by the QuikSCAT daily products for

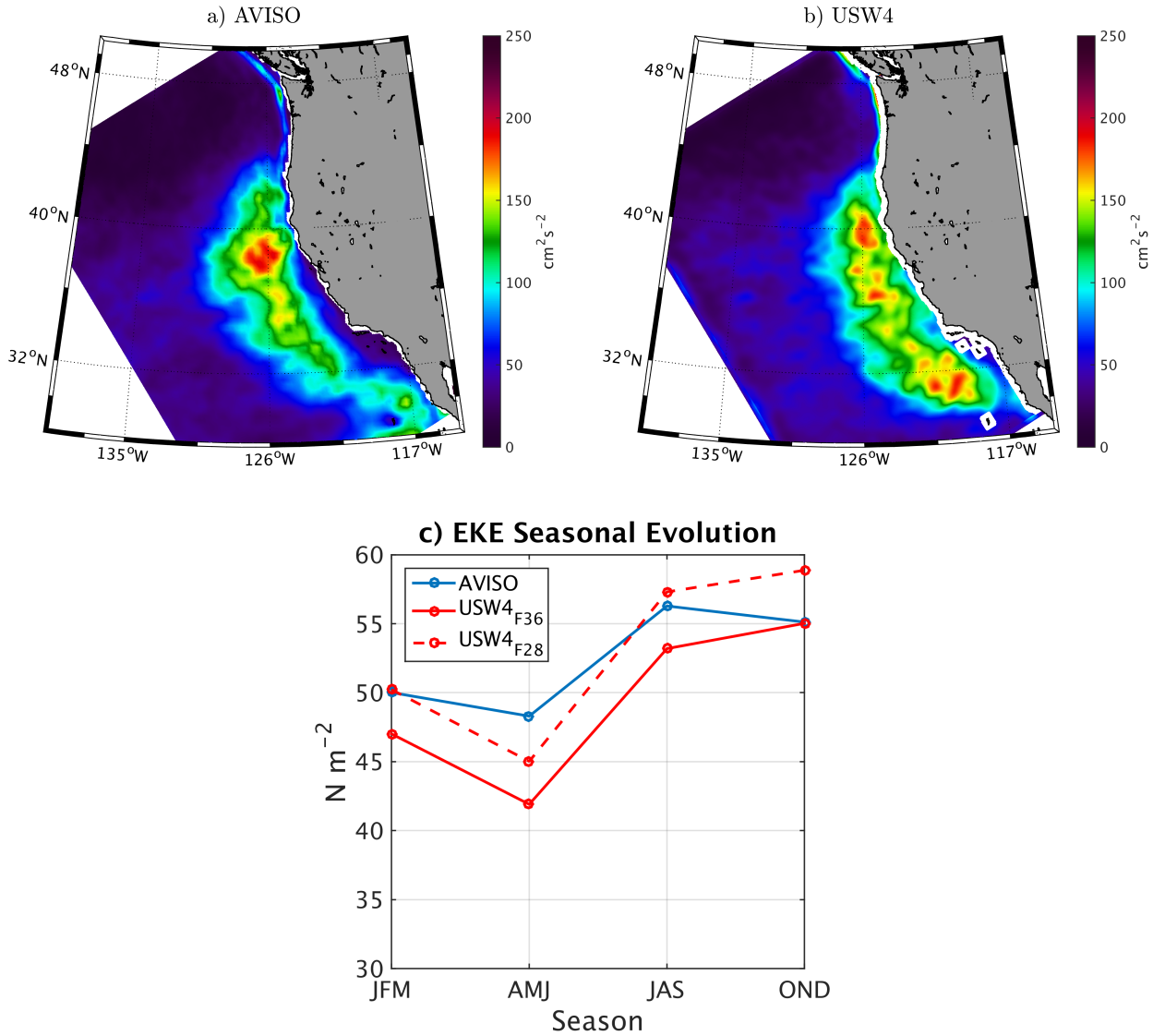


Figure 25: Mean geostrophic surface Eddy Kinetic Energy (EKE) estimated from (a) AVISO and (b) USW4 over the period 1995-2010. The EKE of USW4 is computed using low-pass filtered geostrophic velocities (a Gaussian spatial filter with 36-km-half-width) as an approximate match to AVISO's spatial resolution. (c) Seasonal evolution of the mean EKE averaged over the whole domain as estimated from the observations and from the USW4 filtered velocity, based on two different filter half-widths: 36 km (solid line) and 28 km (dashed line). The current feedback to the atmosphere dampens the eddies and thus allows the simulation to have a realistic EKE level, albeit with not quite the same spatial pattern around the Southern California Bight. Pointwise sampling errors are up to $\approx 5$ cm$^2$ s$^{-2}$, estimated using a bootstrap method (Efron and Tibshirani, 1985): the mean EKE is computed 100,000 times using random samples from the distribution, and the uncertainty is then defined as $\pm$ the standard deviation of these values.

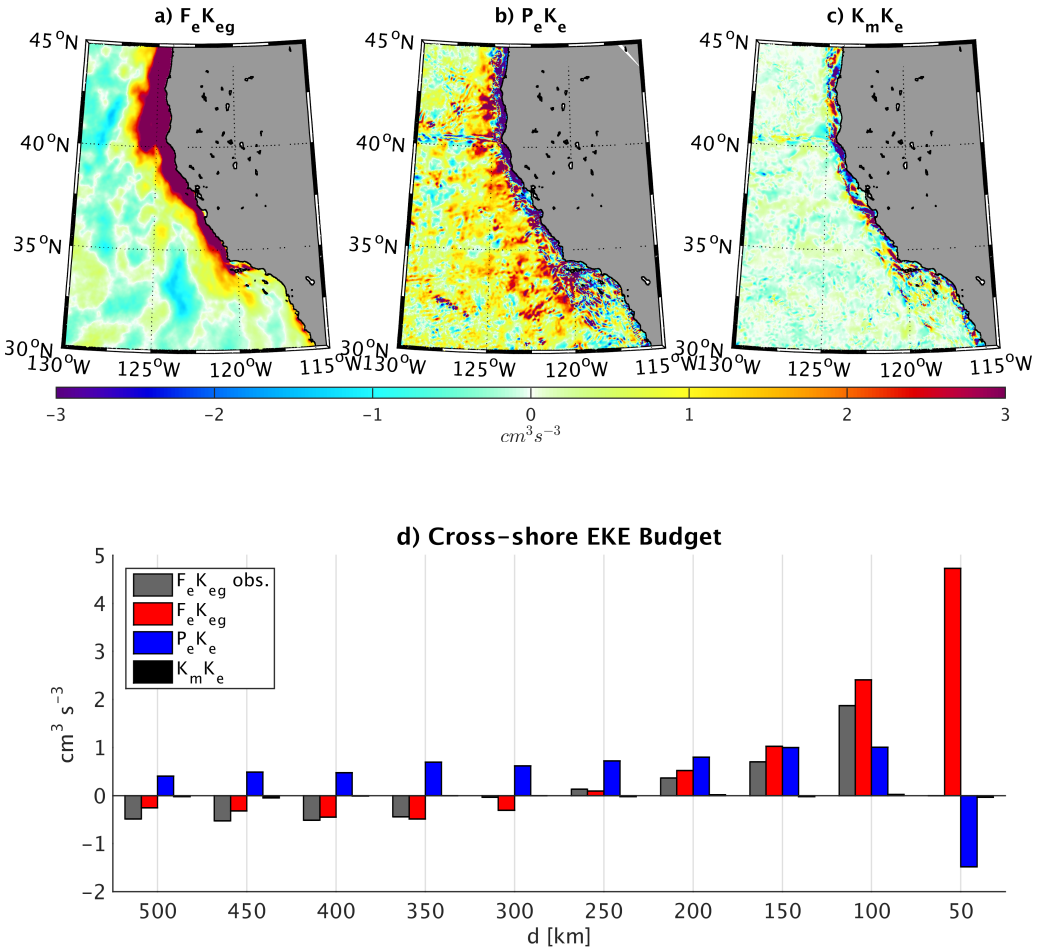


Figure 26: Depth-integrated kinetic energy budget components [cm$^3$ s$^{-3}$] in USW4 over the period 1995-2010: (a)-(c) Geostrophic eddy wind-work ($F_eK_{eg}$), baroclinic conversion ($P_eK_e$), and barotropic conversion from the mean flow ($K_mK_e$). (d) Cross-shore bins of the energy budget components averaged over 50 km intervals between 30°N and 45°N. The geostrophic eddy wind-work ($F_eK_{eg}$) is estimated from USW4 (red) and from observations (QuikSCAT and AVISO; gray). For the first 50 km off the coast the observational estimate is not shown because of coastal contamination. The baroclinic conversion is the main energy generation term. The eddy wind-work $F_eK_{eg}$ is positive nearshore and deflects energy from the ocean to the atmosphere offshore while damping the mesoscale activity.

the CCS. The more striking difference comes from the difference between the mean stress as estimated by USW4 and the one from 1M: the latter's stress is reduced by 60%. The large stress reduction decreases the mean wind-work ($F_mK_{mg}$) by 78%. The larger reduction of $F_mK_{mg}$ is explained by the associated weakening of the surface coastal current (Fig. 27b). From USW4 to 6H and 1D, the surface current is slightly reduced by 7% and 13%, respectively, and from USW4 to 1M, it is reduced by 26%.

Table 1: Mean EKE, surface stress, and alongshore surface current averaged along a coastal band 100 km wide for USW4 (1H forcing) and the three additional experiments using a 6-hourly-averaged wind forcing (6H), a daily-averaged wind forcing (1D), and a monthly-averaged wind forcing (1M).

| | $EKE_{along}$ [cm$^2$ s$^{-2}$] | $\tau_{along}$ [N m$^{-1}$] | $V_{along}$ [cm s$^{-1}$] |
|---|---|---|---|
| 1H | 150 | -0.049 | -5.3 |
| 6H | 144 | -0.049 | -4.9 |
| 1D | 140 | -0.047 | -4.6 |
| 1M | 57 | -0.020 | -2.9 |

The error in wind-work has important consequences on the mesoscale activity. As shown in Fig. 26, the main sources of EKE are the baroclinic energy conversion and the eddy wind-work. By reducing the mean input of energy $F_mK_{mg}$ and the shear of the alongshore current, the absence of the high frequency component of the wind leads to a reduction of the baroclinic conversion rate, $P_eK_e$, by 1%, 4%, and 60% from USW4 when the wind is temporally smoothed to 6H, 1D, and 1M, respectively. The positive coastal $F_eK_{eg}$ is also reduced by 3%, 8%, and 70% (not shown). As a result the mean alongshore EKE is reduced by 4%, 7%, and 62% in wind-smoothings of 6H, 1D, and 1M compared to USW4 (Table 1). A simulation forced by a QuikSCAT product, as in Capet et al. (2008a) and Renault et al. (2016a), likely underestimates the EKE by 7%. An oceanic model could also be forced by a monthly stress (estimated from averaging the hourly stress and thus accumulating the nonlinear effect of synoptic wind); such a simulation would neglect the negative wind-work $F_eK_{eg}$, leading to an overestimation of the EKE by 60% (Fig. 26).

Along a coastline, the cross-shore Ekman transport is proportional to the surface stress, $T_E = \tau_{alongshore}/\rho f$. Thus, the underestimation of the stress by neglecting the high frequency wind leads to a similar underestimation of the transport. The mean Ekman transport is reduced by 2%, 6%, and 60% from USW4 to more smoothly varying winds with 6H, 1D, and 1M averages, respectively.

A striking difference between USW4 and the other simulations is the level of activity in the inertial currents (Fig. 28). By neglecting the hourly stress the inertial currents are much weaker with 1D wind forcing. This is confirmed by the spectrum of the alongshore current: USW4 has a large peak of energy around 18 hours that is not reproduced by 1D. This is consistent with *e.g.,* Zhai (2017), who found that almost all the energy flux from the wind to near-inertial motions in the mid-latitude North Pacific and Atlantic are due to a mesoscale atmospheric system with scales less than 1000 km; a high frequency forcing is deemed to be required to represent them. Finally, the lack of inertial currents in 6H and 1D can be seen through the eddy ageostrophic wind-work ($F_eK_{ea}$) estimated over the 5 years of simulation from USW4, 6H, and 1D. The $F_eK_{ea}$ work is underestimated by 20% by neglecting the sub-6-hourly wind variability and underestimated by about 70% without the sub-daily variability. Consistent with Zhai (2017) and D'Asaro (1985,

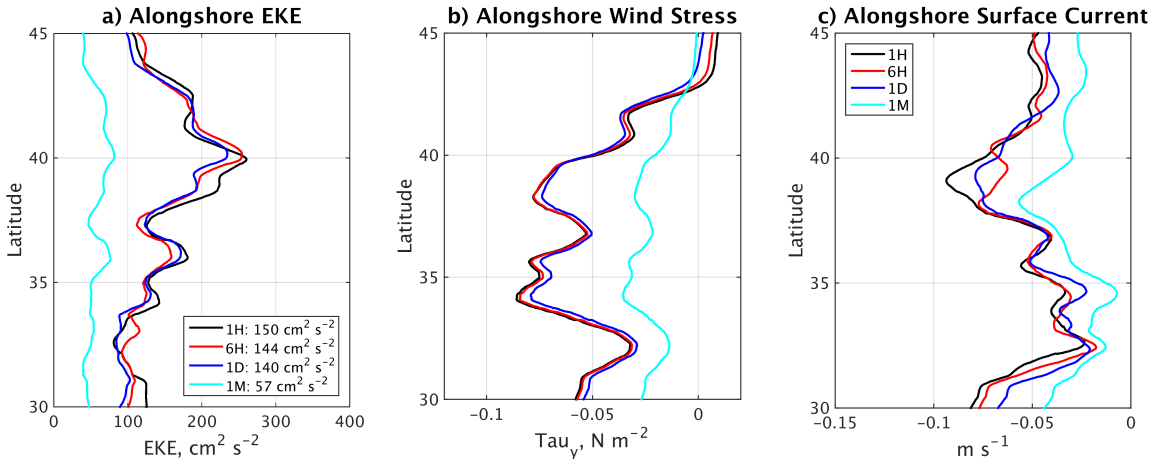


Figure 27: Influence of high-frequency wind forcing on the oceanic surface currents and the surface stress. (a) Annual mean alongshore EKE estimated over a coastal band of 100 km width in USW4 with 1 hr (1H), 6 hr (6H), 1 day (1D), and 1 month (1M) wind update intervals over the period 1995-1999. (b) Same as (a) but for the mean alongshore wind stress. (c) Same as (a) but for the mean alongshore surface current.

1995), the occurrence of winter storms induces larger inertial currents and $F_e K_{ea}$ than during the summer.

# 5 Discussion

In this study regional atmospheric and oceanic model simulations are made for a 16-year reanalysis period from 1995 to 2010. The answers are evaluated against satellite and *in situ* observations with an emphasis on the seasonal cycle and the mean and mesoscale circulations of the California Current System (CCS).

We evaluate the atmospheric forcing simulated by WRF and find, in general, a good agreement between the simulations and the observations of the cloud cover, heat fluxes, and surface stress with modest discrepancies that are some combination of estimation errors and model biases. In particular, we show the ability of the atmospheric model to represent realistically the stratocumulus cloud deck in the northeastern Pacific. Then, by comparing the oceanic simulation to available observations and previous modeling studies, we demonstrate the consistency of the simulations in representing the mean circulation and the seasonal and mesoscale variability of the CCS. Our results illustrate the benefits of using both oceanic and atmospheric regional simulations to simulate the seasonal variability of an eastern boundary upwelling system, at least in part because of the excessively coarse resolution in global models. Although some aspects of the interannual variability have been included in this study, more could be examined about low-frequency variability in the CCS.

The wind drop-off characteristics of a similar atmospheric simulation have been validated by Renault et al. (2016b). The simulation reported in this paper presents a good agreement with the mean circulation as estimated from the CNES-CLS13 dataset, with the California Undercurrent structure as described in the literature, and with the mesoscale activity as estimated from AVISO.

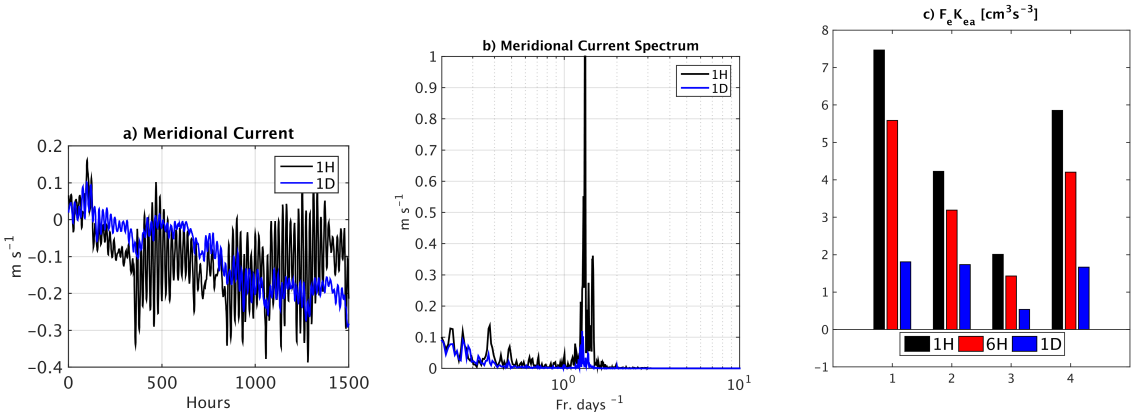


Figure 28: Surface current responses to hourly and daily wind forcing. (a) Hourly time series of the surface meridional current at (36°N, 122°W) (central California coast). The black and blue lines represent the simulation forced by the hourly- (1H, as in the USW4 simulation) and the daily-updated wind (1D). (b) The temporal spectrum of the surface meridional current from the 1H (black) and 1D (blue) simulations at (36°N, 122°W). (c) Mean ageostrophic eddy wind-work ($F_eK_{ea}$) (cm$^3$ s$^{-3}$) averaged between 30°N and 45°N and over a 500 km cross-shore distance from the coast in the 1H, 6H, and 1D simulations. As expected, the high-frequency wind forcing enhances the ageostrophic wind-work and inertial currents.

These oceanic validations are also an indirect validation of the wind profiles simulated by WRF. An alternative simulation has been carried out using the CFSR reanalysis (Saha et al., 2010). Due to a poor representation of the wind drop-off, this simulation was characterized by an unrealistic poleward surface current and a poor representation of the mesoscale activity. The coarse resolution of CFSR (or other similar reanalysis) prevents using such a product to force this particular upwelling region and should not be used to investigate processes or trends, at least in the CCS.

Although not discussed here in any detail, the oceanic simulation is forced using various lateral open-ocean boundary forcing fields, such as Mercator or SODA. Differences in the lateral conditions can lead to significant changes in mean temperature and salinity (up to 0.5°C in SST and 0.5 PSU in $S$). Probably they are the primary cause for the the salinity biases present in the USW4 simulation, which are perhaps the largest inaccuracy of the simulation. We finally chose to force the simulations using Mercator with an additional mean monthly state correction toward the observations from the World Ocean Database over the period 1995-2004. Nevertheless, uncertainty in open ocean boundary conditions of the gyre-scale currents, density, and other water-mass properties do limit the possible accuracy of these quantities in a regional simulation.

An important contribution of this paper is our use over a long time period (1995-2010) of the parameterization of the wind and stress response to the current feedback suggested by Renault et al. (2016d) for the U.S. West Coast. Long-term comparisons with satellite observations show realistic simulation results for the EKE and the energy transfer between the ocean and atmosphere with this feedback — and falsely large EKE values without it — in high-resolution models. Oceanic models, if uncoupled, should take into account the current feedback and by including a parameterization of the wind response such as Eq.(3) for a realistic kinetic energy transfer between the atmosphere and the ocean, and thus for a realistic level of mesoscale activity and mean circulation.

Finally, we discussed the importance of using a high-frequency wind forcing to represent the

mean features of the CCS. In particular, consistent with Wu et al. (2016), we show the presence of high frequency wind prevents using monthly wind to force an ocean model of the CCS. It leads to large errors in the mean stress and wind-work inputs to the ocean, and, thus, to a poor representation of the mean and mesoscale currents. For the CCS we show that a 6-hourly wind forcing realistically the mean surface stress and the mean and mesoscale geostrophic currents. A daily wind forcing, such as QuikSCAT (commonly used to force an ocean model), leads to an underestimation of the EKE by 7% for the CCS, and a monthly forcing is much worse. However, a 1-hourly wind forcing is necessary for proper representation of the inertial currents.

In summary, we show the benefit of using both oceanic and atmospheric simulations for representing the mean physical state of the California Current System. The atmospheric model is characterized by several biases such as too dry a lower atmosphere, too few clouds nearshore (although it realistically represents the stratocumulus cloud deck in the north of the domain), too much precipitation, and slightly too low a surface stress. As a response, the oceanic model has too large a surface salinity, too cold a SST, and too deep a MLD. Some other oceanic biases are controlled by the open-boundary conditions, such as the too-cold 150 m depth temperature. Perfect model-measurement agreement is an impossible goal both because of sampling limitations in model and observational data and because there are too many model design options and parameterization choices to ever be fundamentally correct or precise (McWilliams, 2007). Nevertheless, the USW4 system presented here is in fairly good overall agreement with the observations that exist, and it has no glaring failures with respect to its primary behaviors. It thus provides a reliable physical foundation for assessing biogeochemical cycles and climate changes in the CCS (Deutsch et al., 2019a).

**Codes and Simulation Data** The physical and biogeochemical codes used for our simulations are at *https://github.com/UCLA-ROMS/Code*. The simulation model output archive data can be made available by an email request to the Corresponding Authors.

**Acknowledgments** We appreciate support from the Office of Naval Research (ONR N00014-12-1-0939), the National Science Foundation (OCE-1419450), the California Ocean Protection Council grant (Integrated modeling assessments and projections for the California Current System), the Bureau of Ocean Energy Management, and the National Oceanic and Atmospheric Administration (DOC-NOAA NA15NOS4780186). Model simulations were carried out using the Extreme Science and Engineering Discovery Environment (XSEDE) and Yellowstone computers supported by the National Science Foundation at San Diego Supercomputer Center and NCAR, respectively. This study has been conducted using E.U. Copernicus Marine Service Information. MODIS level 2 data were downloaded from the NASA Web site (available at *http://ladsweb.nascom.nasa.gov*). GPCP data were provided by the NOAA/OAR/ESRL PSD, Boulder, Colorado, USA, from their web site at *https://www.esrl.noaa.gov/psd/*.

# References


1. Adler, R. F., and Coauthors, 2003: The version-2 global precipitation climatology project (GPCP) monthly precipitation analysis (1979–present). *J. Hydromet.*, **4**, 1147–1167.

2. Bednarsek, N., and M. Ohman, 2015: Changes in pteropod distributions and shell dissolution across a frontal system in the California Current System. *Mar. Ecol. Progr. Ser.*, **523**, 93–103.

3. Bednarsek, N., and Coauthors, 2017: Exposure history determines pteropod vulnerability to ocean acidification along the US West Coast. *Sci. Rpts.*, **7**, 4526.

4. Bentamy, A., and D. C. Fillon, 2012: Gridded surface wind fields from Metop/ASCAT measurements. *Int. J. Remote Sensing*, **33**, 1729–1754.

5. Bograd, S. J., D. A. Checkley, and W. S. Wooster, 2003: CalCOFI: A half century of physical, chemical, and biological research in the California Current System. Elsevier.

6. Bopp, L., M. Lévy, L. Resplandy, and J.-B. Sallée, 2015: Pathways of anthropogenic carbon subduction in the global ocean. *Geophys. Res. Lett.*, **42**, 6416–6423.

7. Capet, X., F. Colas, P. Penven, P. Marchesiello, and J. C. McWilliams, 2008a: Eddies in eastern-boundary subtropical upwelling systems. *Ocean Modeling in an Eddying Regime, Geophys. AGU Monogr. Ser*, M. Hecht, and H. Hasumi, Eds., Vol. 177, AGU, 131–147.

8. Capet, X., J. McWilliams, M. Molemaker, and A. Shchepetkin, 2008b: Mesoscale to submesoscale transition in the California Current System. Part i: Flow structure, eddy flux, and observational tests. *J. Phys. Ocean.*, **38**, 29–43.

9. Carr, M.-E., and E. J. Kearns, 2003: Production regimes in four Eastern Boundary Current Systems. *Deep Sea Res. II*, **50**, 3199–3221.

10. Carton, J. A., and B. S. Giese, 2008: A reanalysis of ocean climate using simple ocean data assimilation (SODA). *Mon. Weat. Rev.*, **136**, 2999–3017.

11. Centurioni, L., J. Ohlmann, and P. P. Niiler, 2008: Permanent meanders in the California Current System. *J. Phys. Ocean.*, **38**, 1690–1710.

12. Chan, F., J. Barth, J. Lubchenco, A. Kirincich, H. Weeks, W. T. Peterson, and B. Menge, 2008: Emergence of anoxia in the California Current large marine ecosystem. *Science*, **319**, 920–920.

13. Chavez, F. P., and M. Messie, 2009: A comparison of eastern boundary upwelling ecosystems. *Progr. Oceanogr.*, **83**, 80–96.

14. Chelton, D. B., 1984: Seasonal variability of alongshore geostrophic velocity off central California. *J. Geophys. Res. Oceans*, **89**, 3473–3486.

15. Chelton, D. B., and M. G. Schlax, 2003: The accuracies of smoothed sea surface height fields constructed from tandem satellite altimeter datasets. *J. Ocean. Atmos. Tech.*, **20**, 1276–1302.

16. Chelton, D. B., M. G. Schlax, M. H. Freilich, and R. F. Milliff, 2004: Satellite measurements reveal persistent small-scale features in ocean winds. *Science*, **303**, 978–983.

17. Chen, R., G. R. Flierl, and C. Wunsch, 2014: A description of local and nonlocal eddy–mean flow interaction in a global eddy-permitting state estimate. *J. Phys. Ocean.*, **44**, 2336–2352.

18. Chen, R., J. McWilliams, L. Renault, F. Kessouri, and C. Deutsch, 2019: California Undercurrent: Identification, spatiotemporal variability and biogeochemical consequences. *J. Phys. Ocean.*, in preparation.

19. Chenillat, F., P. Rivière, X. Capet, E. D. Lorenzo, and B. Blanke, 2012: North Pacific Gyre oscillation modulates seasonal timing and ecosystem functioning in the California Current upwelling system. *Geophys. Res. Lett.*, **39**, L01 606.

20. Chhak, K., and E. DiLorenzo, 2007: Decadal variations in the California Current upwelling cells. *Geophys. Res. Lett.*, **34**, L14 604.

21. Chou, M.-D., and M. J. Suarez, 1994: An efficient thermal infrared radiation parameterization for use in general circulation models. *NASA Tech. Memo*, **104606**, 85.

22. Collins, C., L. Ivanov, and O. Melnichenko, 2003: Seasonal variability of the California Undercurrent xtracted from the RAFOS 19922002. *Marine Hydrophys. J.*, **2**, 24–33.

23. Collins, C. A., L. M. Ivanov, O. V. Melnichenko, and N. Garfield, 2004: California Undercurrent variability and eddy transport estimated from RAFOS float observations. *J. Geophys. Res. Oceans*, **109**.

24. Condron, A., and I. A. Renfrew, 2013: The impact of polar mesoscale storms on northeast Atlantic Ocean circulation. *Nat. Geo.*, **6**, 34–37.

25. Dai, A., T. Qian, K. E. Trenberth, and J. D. Milliman, 2009: Changes in continental freshwater discharge from 1948 to 2004. *J. Climate*, **22**, 2773–2792.

26. D'Asaro, E. A., 1985: The energy flux from the wind to near-inertial motions in the surface mixed layer. *J. Phys. Ocean.*, **15**, 1043–1059.

27. D'Asaro, E. A., 1995: Upper-ocean inertial currents forced by a strong storm. part ii: Modeling. *J. Phys. Ocean.*, **25**, 2937–2952.

28. Davis, A., and E. DiLornezo, 2015: Interannual forcing mechanisms of California Current transports I: Meridional Currents. *Deep-Sea Res. II*, **112**, 18–30.

29. de Boyer Montégut, C., G. Madec, A. S. Fischer, A. Lazar, and D. Iudicone, 2004: Mixed layer depth over the global ocean: An examination of profile data and a profile-based climatology. *J. Geophys. Res. Oceans*, **109**, C12 003.

30. Deutsch, C., H. Frenzel, J. C. McWilliams, L. Renault, F. Kessouri, E. Howard, J.-H. Liang, and D. Bianchi, 2019a: Biogeochemical variability in the California Current System. *Progr. Oceanogr.*, submitted.

31. Deutsch, C., L. Olhsson, L. Renault, J. McWilliams, H. Frenzel, and A. Margolskee, 2019b: Coastal hypoxia modulated by coastal wind patterns. *Global Biogeochem. Cycles*, in preparation.

32. Dewar, W. K., and G. R. Flierl, 1987: Some effects of the wind on rings. *J. Phys. Ocean.*, **17**, 1653–1667.

33. Dong, C., J. C. McWilliams, Y. Liu, and D. Chen, 2014: Global heat and salt transports by eddy movement. *Nat. Com.*, **5**, 3294/1–6.

34. Ducet, N., P.-Y. Le Traon, and G. Reverdin, 2000: Global high-resolution mapping of ocean circulation from TOPEX/Poseidon and ERS-1 and-2. *J. Geophys. Res. Oceans*, **105**, 19 477–19 498.

35. Dudhia, J., 1989: Numerical study of convection observed during the winter monsoon experiment using a mesoscale two-dimensional model. *J. Atmos. Sci.*, **46**, 3077–3107.

36. Duhaut, T. H., and D. N. Straub, 2006: Wind stress dependence on ocean surface velocity: Implications for mechanical energy input to ocean circulation. *J. Phys. Ocean.*, **36**, 202–211.

37. Eden, C., and H. Dietze, 2009: Effects of mesoscale eddy/wind interactions on biological new production and eddy kinetic energy. *J. Geophys. Res. Oceans*, **114**, 2156–2202.

38. Efron, B., and R. Tibshirani, 1985: The bootstrap method for assessing statistical accuracy. *Behaviormetrika*, **12 (17)**, 1–35.

39. Esbensen, S. K., and Y. Kushnir, 1981: *The heat budget of the global ocean: An atlas based on estimates from surface marine observations*. 29, Oregon State University.

40. FAO, 2009: State of the World's Fisheries and Aquaculture 2008. *Food and Agriculture Organization of the United Nations*.

41. Feely, R. A., R. R. Okazaki, W.-J. Cai, N. Bednarsek, S. R. Alin, R. H. Byrne, and A. Fassbender, 2018: The combined effects of acidification and hypoxia on pH and aragonite saturation in the coastal waters of the California Current ecosystem and the northern Gulf of Mexico. *Cont. Shelf Res.*, **152**, 50–60.

42. Feely, R. A., C. L. Sabine, J. M. Hernandez-Ayon, D. Ianson, and B. Hales, 2008: Evidence for upwelling of corrosive" acidified" water onto the continental shelf. *Science*, **320**, 1490–1492.

43. Garcia-Reyes, M., W. J. Sydeman, D. S. Schoeman, R. R. Rykaczewsi, B. Black, A. Smit, and S. Bograd, 2105: Under pressure: Climate change, upwelling, and eastern boundary upwelling ecosystems. *Front. Mar. Sci.*, **2**, 109.

44. Gay, P. S., and T. K. Chereskin, 2009: Mean structure and seasonal variability of the poleward undercurrent off southern California. *J. Geophys. Res. Oceans*, **114**.

45. Gómez-Valdivia, F., A. Parés-Sierra, and A. Laura Flores-Morales, 2017: Semiannual variability of the California Undercurrent along the Southern California Current System: A tropical generated phenomenon. *J. Geophys. Res. Oceans*, **122**, 1574–1589.

46. Grantham, B. A., F. Chan, K. J. Nielsen, D. S. Fox, J. A. Barth, A. Huyer, J. Lubchenco, and B. A. Menge, 2004: Upwelling-driven nearshore hypoxia signals ecosystem and oceanographic changes in the northeast Pacific. *Nature*, **429**, 749–754.

47. Gruber, N., C. Hauri, Z. Lachkar, D. Loher, T. L. Frölicher, and G.-K. Plattner, 2012: Rapid progression of ocean acidification in the California Current System. *Science*, **337**, 220–223.

48. Gruber, N., Z. Lachkar, H. Frenzel, P. Marchesiello, M. Münnich, J. C. McWilliams, T. Nagai, and G.-K. Plattner, 2011: Eddy-induced reduction of biological production in Eastern Boundary Upwelling Systems. *Nat. Geosci.*, **4**, 787–792.

49. Gulev, S. K., 1994: Influence of space-time averaging on the ocean-atmosphere exchange estimates in the North Atlantic midlatitudes. *J. Phys. Ocean.*, **24**, 1236–1255.

50. Hickey, B., 1998: Coastal oceanography of western North America from the tip of Baja California to Vancouver Island. *The Sea*, A. Robinson, and K. Brink, Eds., Vol. 11, Harvard Press, 345–393.

51. Holdsworth, A. M., and P. G. Myers, 2015: The influence of high-frequency atmospheric forcing on the circulation and deep convection of the Labrador Sea. *J. Climate*, **28**, 4980–4996.

52. Hong, S.-Y., and J.-O. J. Lim, 2006: The wrf single-moment 6-class microphysics scheme (wsm6). *J. Korean Meteor. Soc*, **42**, 129–151.

53. Jacox, M. G., J. Fiechter, A. M. Moore, and C. A. Edwards, 2015: ENSO and the California Current coastal upwelling response. *J. Geophys. Res. Oceans*, **120**, 1691–1702.

54. Jousse, A., A. Hall, F. Sun, and J. Teixeira, 2016: Causes of wrf surface energy fluxes biases in a stratocumulus region. *Climate Dynamics*, **46**, 571–584.

55. Kosro, P., 2002: A poleward jet and an equatorward undercurrent observed off oregon and northern california, during the 1997–98 el nino. *Progress in Oceanography*, **54 (1-4)**, 343–360.

56. Large, W., and S. Yeager, 2009: The global climatology of an interannually varying air–sea flux data set. *Clim. Dyn.*, **33**, 341–364.

57. Large, W. B., 2006: Surface fluxes for practitioners of global ocean data assimilation. *Ocean Weat. For.*, Springer, 229–270.

58. Large, W. G., J. C. McWilliams, and S. C. Doney, 1994: Oceanic vertical mixing: A review and a model with a nonlocal boundary layer parameterization. *Rev. Geophys.*, **32**, 363–404.

59. Lemarié, F., J. Kurian, A. F. Shchepetkin, M. J. Molemaker, F. Colas, and J. C. McWilliams, 2012: Are there inescapable issues prohibiting the use of terrain-following coordinates in climate models? *Ocean Modelling*, **42**, 57–79.

60. Locarnini, R., and Coauthors, 2013: World Ocean Atlas 2013: Temperature. *NOAA NESDIS*, **1**.

61. Lorenzo, E. D., and Coauthors, 2009: Nutrient and salinity decadal variations in the central and eastern North Pacific. *Geophys. Res. Lett.*, **36**, L14 601.

62. Lynn, R., and J. Simpson, 1990: The flow of the undercurrent over the continental borderland off southern california. *J. Geophys. Res. Oceans*, **95**, 12 995–13 008.

63. Lynn, R. J., and S. J. Bograd, 2002: Dynamic evolution of the 19971999 El NioLa Nia cycle in the southern California Current System. *Progr. Oceanogr.*, **54**, 59–75.

64. Lynn, R. J., and J. J. Simpson, 1987: The California Current System: The seasonal variability of its physical characteristics. *J. Geophys. Res. Oceans*, **92**, 12 947–12 966.

65. Marchesiello, P., J. C. McWilliams, and A. Shchepetkin, 2003: Equilibrium structure and dynamics of the California Current System. *J. Phys. Ocean.*, **33**, 753–783.

66. McCreary, J. P., and S.-Y. Chao, 1985: Three-dimensional shelf circulation along an eastern ocean boundary. *J. Mar. Res.*, **43**, 13–36.

67. McCreary, J. P., P. K. Kundu, and S.-Y. Chao, 1987: On the dynamics of the California Current System. *J. Mar. Res.*, **45**, 1–32.

68. McGillicuddy, D. J., 2016: Mechanisms of physical-biological-biogeochemical interaction at the oceanic mesoscale. *Annu. Rev. Marine. Sci.*, **8**, 125–159.

69. McWilliams, J. C., 2007: Irreducible imprecision in atmospheric and oceanic simulations. *Proc. Nat. Acad. Sci.*, **104**, 8709–8713.

70. Meinvielle, M., and G. C. Johnson, 2013: Decadal water-property trends in the California Undercurrent, with implications for ocean acidification. *J. Geophys. Res. Oceans*, **118**, 6687–6703.

71. Molemaker, M. J., J. C. McWilliams, and W. K. Dewar, 2015: Submesoscale instability and generation of mesoscale anticyclones near a separation of the California Undercurrent. *J. Phys. Ocean.*, **45**, 613–629.

72. Nam, C., S. Bony, J.-L. Dufresne, and H. Chepfer, 2012: The too few, too bright tropical low-cloud problem in CMIP5 models. *Geophys. Res. Lett.*, **39**.

73. Pennington, J. T., K. L. Mahoney, V. S. Kuwahara, D. D. Kolber, R. Calienes, and F. P. Chavez, 2006: Primary production in the eastern tropical Pacific: A review. *Progr. Oceanogr.*, **69**, 285–317.

74. Pierce, S., R. Smith, P. Kosro, J. Barth, and C. Wilson, 2000: Continuity of the poleward undercurrent along the eastern boundary of the mid-latitude north Pacific. *Deep-Sea Res. II*, **47**, 811–829.

75. Platnick, S., M. D. King, S. A. Ackerman, W. P. Menzel, B. A. Baum, J. C. Riédi, and R. A. Frey, 2003: The MODIS cloud products: Algorithms and examples from terra. *IEEE Trans. Geosci. and Remote Sensing*, **41**, 459–473.

76. Rapp, A. D., M. Lebsock, and T. LEcuyer, 2013: Low cloud precipitation climatology in the southeastern Pacific marine stratocumulus region using CloudSat. *Environ. Res. Lett.*, **8**, 014 027.

77. Renault, L., C. Deutsch, J. C. McWilliams, H. Frenzel, J.-H. Liang, and F. Colas, 2016a: Partial decoupling of primary productivity from upwelling in the California Current System. *Nat. Geosci.*, **9**, 505–508.

78. Renault, L., B. Dewitte, M. Falvey, R. Garreaud, V. Echevin, and F. Bonjean, 2009: Impact of atmospheric coastal jet off central Chile on sea surface temperature from satellite observations (2000–2007). *J. Geophys. Res.: Oceans (1978–2012)*, **114**.

79. Renault, L., A. Hall, and J. C. McWilliams, 2016b: Orographic shaping of U.S. West Coast wind profiles during the upwelling eeason. *Clim. Dyn*, 1–17.

80. Renault, L., J. C. McWilliams, and P. Penven, 2017: Modulation of the Agulhas Current retroflection and leakage by oceanic current interaction with the atmosphere in coupled simulations. *J. Phys. Ocean.*, **47**, 2077–2100.

81. Renault, L., M. J. Molemaker, J. Gula, S. Masson, and J. C. McWilliams, 2016c: Control and stabilization of the Gulf Stream by oceanic current interaction with the atmosphere. *J. Phys. Ocean.*, **46**, 3439–3453.

82. Renault, L., M. J. Molemaker, J. C. McWilliams, A. F. Shchepetkin, F. Lemarié, D. Chelton, S. Illig, and A. Hall, 2016d: Modulation of wind work by oceanic current interaction with the atmosphere. *J. Phys. Ocean.*, **46**, 1685–1704.

83. Renault, L., and Coauthors, 2012: Upwelling response to atmospheric coastal jets off central Chile: A modeling study of the October 2000 event. *J. Geophys. Res. Oceans*, **117**, C02 030.

84. Richter, I., 2015: Climate model biases in the eastern tropical oceans: causes, impacts and ways forward. *Wiley Interdisciplinary Reviews: Climate Change*, **6**, 345–358.

85. Ridgway, K., J. Dunn, and J. Wilkin, 2002: Ocean interpolation by four-dimensional weighted least squares-application to the waters around Australasia. *J. Ocean. Atmos. Tech.*, **19**, 1357–1375.

86. Rio, M., S. Mulet, and N. Picot, 2013: New global mean dynamic topography from a GOCE geoid model, altimeter measurements and oceanographic in-situ data. *Proceedings of the ESA Living Planet Symposium, Edinburgh*.

87. Rio, M.-H., S. Mulet, and N. Picot, 2014: Beyond GOCE for the ocean circulation estimate: Synergetic use of altimetry, gravimetry, and in situ data provides new insight into geostrophic and ekman currents. *Geophys. Res. Lett.*, **41**, 8918–8925.

88. Risien, C. M., and D. B. Chelton, 2008: A global climatology of surface wind and wind stress fields from eight years of QuikSCAT scatterometer data. *J. Phys. Ocean.*, **38**, 2379–2413.

89. Ryan, H., and M. Noble, 2002: Sea level response to enso along the central california coast: how the 1997–1998 event compares with the historic record. *Progress in Oceanography*, **54 (1-4)**, 149–169.

90. Saha, S., and Coauthors, 2010: The NCEP climate forecast system reanalysis. *Bull. Am. Meteor. Soc.*, **91**, 1015–1057.

91. Seo, H., A. J. Miller, and J. R. Norris, 2015: Eddy-wind interaction in the California Current System: Dynamics and impacts. *J. Phys. Ocean.*, **46**, 439–459.

92. Shchepetkin, A. F., 2015: An adaptive, Courant-number-dependent implicit scheme for vertical advection in oceanic modeling. *Ocean Modelling*, **91**, 38–69.

93. Shchepetkin, A. F., and J. C. McWilliams, 2005: The Regional Oceanic Modeling System (ROMS): A split-explicit, free-surface, topography-following-coordinate oceanic model. *Ocean Modelling*, **9**, 347–404.

94. Shchepetkin, A. F., and J. C. McWilliams, 2009: Correction and commentary for ocean forecasting in terrain-following coordinates: Formulation and skill assessment of the regional ocean modeling system by Haidvogel et al., J. Comp. Phys.. 227, pp. 3595–3624. *J. Comput. Phys.*, **228**, 8985–9000.

95. Skamarock, W., J. Klemp, J. Dudhia, D. Gill, and D. Barker, 2008: A description of the Advanced Research WRF version 3. Tech. rep., Note NCAR/TN-4751STR.

96. Spillane, M., D. Enfield, and J. Allen, 1987: Intraseasonal oscillations in sea level along the west coast of the americas. *Journal of Physical Oceanography*, **17 (3)**, 313–325.

97. Stark, J. D., C. J. Donlon, M. J. Martin, and M. E. McCulloch, 2007: Ostia: An operational, high resolution, real time, global sea surface temperature analysis system. *Oceans 2007-Europe*, IEEE, 1–4.

98. Stern, M. E., 1975: *Ocean Circulation Physics*. Academic Press, Inc.

99. Stramma, L., S. Schmidtko, L. A. Levin, and G. C. Johnson, 2010: Ocean oxygen minima expansions and their biological impacts. *Deep-Sea Res. I*, **57**, 587–595.

100. Stramma, L., and Coauthors, 2012: Expansion of oxygen minimum zones may reduce available habitat for tropical pelagic fishes. *Nature Climate Change*, **2**, 33–37.

101. Strub, P. T., and C. James, 2000: Altimeter-derived variability of surface velocities in the California Current System: 2. Seasonal circulation and eddy statistics. *Deep-Sea Res. II*, **47**, 831870.

102. Swenson, M., and P. Niiler, 1996: Statistical analysis of the surface circulation of the California Current. *J. Geophys. Res. Oceans*, **101**, 22 631–22 645.

103. Veneziani, M., C. Edwards, J. Doyle, and D. Foley, 2009: A central California coastal ocean modeling study: Forward model and the influence of realistic versus climatological forcing. *J. Geophys. Res. Oceans*, **114**.

104. Wilson, T. H., and R. G. Fovell, 2016: Modeling the evolution and life cycle of stable cold pools. *Weather and Forecasting*, **31**, 1753–1769.

105. Winant, C., C. Dorman, C. Friehe, and R. Beardsley, 1988: The marine layer off northern California: An example of supercritical channel flow. *J. Atmos. Sci.*, **45**, 3588–3605.

106. Wu, Y., X. Zhai, and Z. Wang, 2016: Impact of synoptic atmospheric forcing on the mean ocean circulation. *J. Climate*, **29**, 5709–5724.

107. Wunsch, C., 1999: Where do ocean eddy heat fluxes matter? *J. Geophys. Res. Oceans*, **104**, 13.

108. Wyant, M. C., and Coauthors, 2010: The PreVOCA experiment: modeling the lower troposphere in the Southeast Pacific. *Atmos. Chem. Phys.*, **10**, 4757–4774.

109. Zermeño-Díaz, D. M., C. Zhang, P. Kollias, and H. Kalesse, 2015: The role of shallow cloud moistening in MJO and non-MJO convective events over the ARM Manus site. *J. Atmos. Sci.*, **72**, 4797–4820.

110. Zhai, X., 2013: On the wind mechanical forcing of the ocean general circulation. *J. Geophys. Res. Oceans*, **118**, 6561–6577.

111. Zhai, X., 2017: Dependence of energy flux from the wind to surface inertial currents on the scale of atmospheric motions. *J. Phys. Ocean.*, **47**, 2711–2719.

112. Zhai, X., H. L. Johnson, D. P. Marshall, and C. Wunsch, 2012: On the wind power input to the ocean general circulation. *J. Phys. Ocean.*, **42**, 1357–1365.

113. Zweng, M., and Coauthors, 2013: World Ocean Atlas 2013,: Salinity. *NOAA NESDIS*, **2**.